NORTHWESTERN UNIVERSITY

A Comprehensive Investigation of Type IIb Supernova Progenitors: Combining Theory, Observations, and Statistics

A DISSERTATION

SUBMITTED TO THE GRADUATE SCHOOL
IN PARTIAL FULFILLMENT OF THE REQUIREMENTS

for the degree

DOCTOR OF PHILOSOPHY

Field of Physics and Astronomy

By

Niharika Sravan

EVANSTON, ILLINOIS

September 2018

ABSTRACT

A Comprehensive Investigation of Type IIb Supernova Progenitors: Combining Theory, Observations, and Statistics

Niharika Sravan

Context: Type IIb supernovae (SNe) are important candidates to understand mechanisms that drive the stripping of stripped-envelope (SE) supernova (SN) progenitors. While binary interactions and their high incidence are generally cited to favor them as Type IIb SN progenitors, this idea has not been tested using models covering a broad parameter space.

Aims: In this work we use single- and binary-star models at solar and low metallicities covering a broad parameter space to investigate the progenitors of and evolutionary pathways to Type IIb SNe. We also estimate theoretical Type IIb SN rates and make predictions for observable constraints. We also perform a case study on SN 2016gkg using Bayesian inference to derive the probability distributions of its progenitors using existing observational constraints.

Methods: We use the largest database of self-consistently computed Type IIb progenitor models, statistical inference methods and multiple comparison methods to observations. As a result, our work provides the strongest constraints on Type IIb progenitors and progenitor channels to date.

Results: We find that the parameter space for single-star SN IIb progenitors decreases and that for binary-star SN IIb progenitors increases with decreasing metallicity.

We find that single and binary stars contribute roughly the same as Type IIb SNe at solar metallicity. Binary stars only dominate as progenitors at low metallicity. We also find that our models can account for less than half the observationally inferred rate for Type IIb SNe at high metallicity, making up $< 4.5\%$ of all core-collapse (CC) SNe. On the other hand, our models can account for the rates currently indicated by observations at low metallicity, making up $0.5 - 15\%$ of all CC SNe. However, this requires low mass transfer efficiencies (~ 0.1) in the binaries.

We find that potential binary star progenitors for SN 2016gkg have smaller pre-SN hydrogen-envelope and helium-core masses than potential single-star progenitors typically by $0.1 M_\odot$ and $2 M_\odot$, respectively. We find that, a binary companion, if present, is a main-sequence or red-giant star. We demonstrate that the range of progenitor helium-core mass for SN 2016gkg inferred from observations could help improve constraints on the progenitor. We find that the probability that the progenitor of SN 2016gkg was a binary is 22% when we use constraints only on the progenitor luminosity and effective temperature. Imposing the range of pre-SN progenitor hydrogen-envelope mass and radius inferred from SN light-curves the probability the progenitor is a binary increases to 44%. However, there is no clear preference for a binary progenitor.

Conclusions: We suggest that, at solar metallicity, the stellar wind mass-loss rates are lower than those currently used in most stellar evolution models. Lower mass-loss rates would widen the parameter space for binary Type IIb SNe at solar metallicity by allowing stars that initiate mass transfer earlier in their evolution to reach CC without getting stripped. Our analysis of SN 2016gkg demonstrates the importance of statistical inference methods to constrain progenitor channels. Our work indicates that to address the question of progenitors of SNe IIb we still need four pieces of information: (1) SN IIb rates as a function of metallicity, (2) better constraints on structural properties of SN IIb progenitors, (3) robust distributions for single- and binary- star properties, and (4) theoretical models for SN IIb progenitors at solar metallicity using the 'correct' mass-loss prescription. Finally, our work highlights the importance of self-consistent broad parameter space modeling and statistical inference methods to constrain SN progenitor channels. Such methods will be especially important given the deluge of data expected with the imminent launch of Large Synoptic Survey Telescope (LSST).

Table of Contents

List of Tables

List of Figures

CHAPTER 1

Introduction

1.1. An Overview of Type IIb SNe

Core-collapse SNe are explosions marking deaths of stars with zero-age main sequence (ZAMS) masses $\gtrsim 8M_{\odot}$ (see e.g. Smartt, 2009, for a recent review). Depending on the absence or presence of hydrogen lines in supernova spectrum, SNe are classified into Type I or Type II, respectively. The absence of hydrogen features in a Type I CC SN spectrum is attributed to a progenitor star that lacks its outer hydrogen layers. Type IIb SN progenitors exhibit 'mild' stripping of their outer layers, initially exhibiting prominent hydrogen spectral features that weaken and disappear in the weeks following the explosion. Type I CC (also known as Type Ibc) and Type IIb SNe are therefore also referred to as SE SNe. The mechanisms that drive the stripping and regimes in which they dominate are still open questions. The leading candidates are close binary interactions (e.g., Podsiadlowski et al., 1992; Yoon et al., 2010, 2017), stellar winds (e.g., Woosley et al., 1993; Georgy et al., 2012; Groh et al., 2013b), stellar rotation (e.g., Georgy et al., 2012; Groh et al., 2013a,b), and nuclear burning instabilities (e.g., Arnett & Meakin, 2011; Strotjohann et al., 2015).

Binary interactions were initially the favored channel to strip stars due to the high observed binarity of Wolf-Rayet stars. However, with spectroscopic UV observations indicating strong stellar winds that were sufficient to strip stars (Chiosi et al., 1978), they became the preferred channel. The trend is now appearing to be reversing, with binary interactions gaining traction as the preferred formation channel. This is due a variety of pieces of evidence. First, clumping in stellar winds suggest that currently used mass-loss rates are too high; hot wind mass-loss rates are lower by a factor of $2-3$ than currently used in stellar evolution calculations (Smith 2014; but also see Vink & Gräfener 2012). Second, recent observations indicate that massive stars are predominantly part of close binary systems (Sana et al., 2012; Moe & Di Stefano, 2017). Other indirect lines of support for the binary interaction channel to SE SNe include the fact that observed SE SN rates are too high to be explained solely by single-star evolution (Smith et al., 2011) and very high inferred mass-loss rates for SE SN progenitors from X-ray/radio observations (Wellons et al., 2012; Drout et al., 2016).

Type IIb SNe are of particular interest in understanding formation channels to SE SNe because of a few reasons. First, they are the only class within the group that has several (five) identified progenitors[1]. Second, there is evidence for the presence of a binary companion to the progenitor in some cases (Fox et al., 2014; Folatelli et al., 2014a; Ryder et al., 2018a). Finally, Type IIb SNe are quite abundant, accounting for $10-12\%$ of all CCSNe and 30-40% of all SE SNe (Li et al., 2011; Smith et al., 2011; Shivvers et al., 2017).

[1]The progenitor of Type Ib SN iPTF13bvn was identified by Cao et al. (2013) and confirmed by its disappearance by Folatelli et al. (2016). There is also a candidate for the progenitor of Type Ic SN 2017ein (Van Dyk et al., 2018).

1.2. A Brief History of Type IIb SNe

The classification Type IIb began with SN 1987K in NGC 4651 (Filippenko, 1988). SN 1993J is the prototypical Type IIb SN. It exploded in the nearby spiral galaxy M81. Early light curve modeling of SN 1993J indicated that its progenitor was a helium star having a low-mass and extended residual Hydrogen envelope (Nomoto et al., 1993; Podsiadlowski et al., 1993; Filippenko et al., 1993; Woosley et al., 1994). Its progenitor star was identified in ground-based pre-explosion images by Aldering et al. (1994). They also found that the SED had a blue component which they attributed to either an OB association or a binary companion. Late-time observations of the region provide strong direct evidence for the presence of a companion star (Maund et al., 2004; Fox et al., 2014). SN 1993J is the best-studied Type IIb SN to date, in part due to its proximity, being the subject of several observational and theoretical investigations.

Since 1993, progenitors of four more Type IIb SNe have been identified in pre-explosion images: SN 2008ax (Crockett et al., 2008; Folatelli et al., 2015), SN 2011dh (Maund et al., 2011; Van Dyk et al., 2011; Benvenuto et al., 2013), SN 2013df (Van Dyk et al., 2014; Maeda et al., 2015), and SN 2016gkg (Kilpatrick et al., 2017; Tartaglia et al., 2017; Bersten et al., 2018). There is also evidence for binary companions to the progenitors of SN 2001ig and SN 2011dh (Fox et al., 2014; Ryder et al., 2018a; Folatelli et al., 2014a). The Galactic supernova remnant, Cassiopeia A, is known to be the result of a Type IIb SN from spectra of light echoes (Krause et al., 2008; Rest et al., 2011). There is no bound companion to the progenitor even at deep limits (Kochanek, 2018).

1.3. Past Efforts Towards Understanding the Progenitors of Type IIb SNe

Most early theoretical investigations into progenitors of and evolutionary pathways to Type IIb focussed on SN 1993J (e.g., Podsiadlowski et al., 1993; Woosley et al., 1994; Maund et al., 2004; Stancliffe & Eldridge, 2009). Chevalier & Soderberg (2010) studied a sample of Type IIb SNe and suggested that they can further be classified into two sub-types, compact and extended; compact (extended) Type IIb SNe have compact (extended) progenitors and exhibit high (low) radio shell velocities. However, this suggestion was challenged quickly by the discovery of SN 2011dh exhibiting both rapidly expanding radio shells (Soderberg et al., 2012) and an extended yellow supergiant (YSG) progenitor (Folatelli et al., 2014a). Yoon et al. (2010) and Dessart et al. (2011) studied progenitors of Type Ib/c SNe arising as a result of mass transfer in close binary systems and found that some of their Type Ib SN progenitors exploded with small amounts of residual hydrogen. They suggested that these progenitors may be classified as Type IIb SNe if detected soon after explosion. Indeed, Folatelli et al. (2014b) found that some Type Ib/c SNe were misclassified and are actually Type IIb SNe and, more recently, Liu et al. (2016) found significant overlap and a continuum in the signatures of Type IIb and Ib SNe spectra.

Claeys et al. (2011) performed the first parameter space search for single and binary progenitors of Type IIb SNe and their companions. However, they restricted their binary parameter search space to initial primary masses $15M_{\odot}$, initial secondary masses $10M_{\odot} - 15M_{\odot}$, initial orbital periods $800 - 2100$ days, and solar metallicity. Groh et al. (2013a) and Groh et al. (2013b) used solar-metallicity single-star non-rotating and rotating models and identified their $20-25M_\odot$ rotating models as potential Type IIb SN progenitors. Recently, Yoon et al. (2017) undertook a wide parameter space search for binary Type IIb and Ib SN progenitors, varying the initial primary-star mass from $10-18M_\odot$, initial orbital period from $10-3000$ days, with initial mass ratio $=0.9$ for two different metallicities, $Z=0.007$ and 0.02. They assumed only non-conservative mass transfer with mass transfer efficiency of 0.2.

1.4. Motivations and Goals of Dissertation

The advent of rapid-cadence big-data telescopes like the ZTF (Bellm, 2014; Bellm & Kulkarni, 2017), ASSA-SN (Kochanek et al., 2017), DLT40 (Valenti et al., 2017), KAIT (Filippenko et al., 2001), and, at the turn of the decade, LSST (Tyson, 2002; Ivezic et al., 2008) have created an urgency for a comprehensive database of theoretical models to aid with progenitor characterization and in the case of binary progenitors, their companions. Large Synoptic Survey Telescope (LSST) will collect 30TB of data per night and is expected to find 1-10 million new events per night. This is a factor of 100 higher than the largest current survey, the Palomar Transient Factory (PTF). In turn, the wealth of information that is expected to be available in the future will allow us to test our models and improve our understanding of the physics governing various transient phenomena. Motivated by this need, we investigate the progenitors (their evolutionary pathways and properties) of Type IIb SNe (henceforth referred to as SNe IIb) using a comprehensive parameter space study. We also conduct a comprehensive statistical analysis on SN 2016gkg to derive constraints on its progenitor system as a case study and to test our methods.

CHAPTER 2

Stellar Models

We use Modules for Experiments in Stellar Astrophysics (`MESA` Release 9575; Paxton et al., 2011, 2013, 2015, 2018) to compute a large grid of non-rotating single- and binary-star models at solar ($Z_{\odot}$) and 1/4 solar (which we henceforth refer to as 'low metallicity') metallicities. We choose the latter to represent nearby low metallicity environments, i.e. between the Large and Small Magellanic Cloud metallicities.

2.1. Physics and Numerical Assumptions

We adopt the value[1] of $Z_{\odot} = 0.02$ to allow comparison of our results with earlier studies. We assume that helium abundance increases linearly from its primordial value Y = 0.2477 (Peimbert et al., 2007) at Z = 0.0 to Y = 0.28 at Z = 0.02 (Brott et al., 2011). In the following, we summarize the properties of our models.

We use the `basic.net`, `co_burn.net`, and `approx21.net` nuclear networks in `MESA`. We use radiative opacities tables from the OPAL project (Iglesias & Rogers, 1996) scaled to the initial abundances of a model. We model convection using the standard mixing-length theory (MLT; Böhm-Vitense, 1958; Cox & Giuli, 1968), adopting the Ledoux criterion, with the mixing length parameter, $\alpha_{\rm MLT}$, set to 1.5, However, during late-stages of massive star evolution, regions in convective envelopes can approach the Eddington limit with convective velocities nearing the sound speed,

[1]We note that the exact value of $Z_{\odot}$ is not settled (see e.g., Asplund et al., 2009; Vagnozzi et al., 2017).

which is inconsistent with the assumptions of standard MLT. Since the treatment of the physics in these regimes is a subject of active research, we currently employ a different treatment of convection in `MESA`, known as MLT++ (Section 7.2, Paxton et al., 2013), that artificially reduces the super-adiabacity in these regions, implying unspecified additional energy transport. We model overshooting by extending the hydrogen-burning convective core boundary determined by the Ledoux criterion by 0.335 of $H_{\rm p}$ (Brott et al., 2011). We assume negligible overshooting for all other convective regions. Semi-convection occurs when a region that is unstable according to the Ledoux criterion is stabilized by a composition gradient. It has an important, yet ill-constrained, effect on the evolution of massive stars (Langer, 1991). `MESA` uses the formulation of Langer et al. (1983) to model semi-convection. We adopt the value of the dimensionless free-parameter $\alpha_{\rm sc}$ to be 1.0 (Yoon et al., 2006). Similarly, thermohaline mixing can also cause additional mixing by rendering a region that is stable according to the Ledoux criterion unstable due to a negative composition gradient. This phenomenon has an important effect on the evolution of accretors in close binary systems (e.g., Stancliffe et al., 2007). `MESA` uses the formulation of Kippenhahn et al. (1980) to model thermohaline mixing. We adopt the value of the dimensionless free-parameter $\alpha_{\rm th}$ to be 1.0.

We use luminosity, effective temperature ($T_{\rm eff}$), surface hydrogen mass fraction ($X_{\rm surf}$), and metallicity dependent stellar winds. When $T_{\rm eff} \geq 1.1 \times 10^4$ K we adopt the prescription of Vink et al. (2001) when $X_{\rm surf} \geq 0.4$ and that of Nugis & Lamers (2000) otherwise. When $T_{\rm eff} \leq 10^4$ K we adopt the prescription of de Jager et al. (1988) scaled by $(Z/Z_{\odot})^{0.85}$, to match the metallicity scaling of Vink et al. (2001), where Z is the initial metallicity of a model. Note that the prescription of Nugis & Lamers (2000) scales as the square-root of surface metallicity. When $10^4\,\mathrm{K} < T_{\rm eff} < 1.1 \times 10^4\,\mathrm{K}$ we interpolate between the results for $T_{\rm eff} \geq 1.1 \times 10^4\,\mathrm{K}$ and $T_{\rm eff} \leq 10^4\,\mathrm{K}$.

We use the binary module of `MESA` to model binary stars. We adopt the 'implicit' mass transfer scheme (Paxton et al., 2015) and the prescription of Kolb & Ritter (1990) to compute the mass transfer rate due to Roche-lobe overflow (RLO). The mass lost from the primary due to RLO is transferred to the secondary with an efficiency (ratio of mass accreted by the secondary to the mass transferred via RLO by the primary), ϵ, that we assume to be constant during the entire evolution. We assume that the remaining mass is lost from the vicinity of the accretor as its stellar winds. Stellar winds are assumed to carry away the specific angular momentum of the mass losing stars. We require that primaries transfer at least 1% of their initial mass in RLO to qualify as 'binary' progenitors. This is to exclude effectively non-interacting binary-star models that largely resemble their single star analogs. We show in Section 5 that the exact criterion for selecting 'binaries' does not effect our inferences for progenitor channels and derived rates significantly. Finally, we assume all initial orbits to be circular.

We start the evolution of every star at the zero-age main sequence (ZAMS). We terminate the evolution if any one of these conditions are met: (1) the central carbon mass fraction drops below 10^{-6} for solar-metallicity models and 10^{-3} for low-metallicity models, in which case we assume the star has reached CC[2], (2) if the

[2]After modeling our solar-metallicity models we found we could stop the evolution of our models earlier and used it in our low-metallicity models. See the Appendix where we evolve representative solar- and low-metallicity models to advanced nuclear burning stages.

Table 2.1. Initial properties of solar- and low-metallicity models

		Solar Metallicity			Low Metallicity		
Type	Property	min	max	interval	min	max	interval
Single Stars	$\log_{10}(M_{\rm ZAMS}/M_{\odot})$	1.3445	1.4090	0.0005	1.7	–	–
	$\log_{10}(M_{\rm ZAMS,1}/M_{\odot})$	1.00	1.40	0.02	1.00	1.40	0.02
Binary Stars	$q_{\rm ZAMS}$	0.225	0.975	0.05	0.225	0.975	0.05
					1.0	2.6	0.1
	$\log_{10}(P_{\rm orb}/{\rm d})$	2.5	3.8	0.02		+	
					2.7	3.7	0.02

[1]$M_{\rm ZAMS,1}$: Initial primary mass

[2]$q_{\rm ZAMS} \equiv M_{\rm ZAMS,2}/M_{\rm ZAMS,1}$: Initial mass ratio

[3]$P_{\rm orb}$: Initial orbital period

hydrogen-envelope mass drops below $0.01 M_{\odot}$, in which case we assume the star is stripped and will explode as a Type Ibc SN, or (3), in binaries, the accretor overfills its Roche-lobe, in which case we assume a common-envelope (CE) ensues. We assume the surface properties of the star at this stage match the pre-SN state. While this is plausible, recent work suggests that waves can efficiently transport energy outwards during core neon and oxygen burning stages. This could result in outbursts and large fluctuations in surface properties of the star in the years or months leading to CC (Quataert & Shiode, 2012; Shiode & Quataert, 2014; Fuller, 2017).

2.2. Parameter Space

In the following subsections and Table 2.1 we summarize the parameter space for our single- and binary-star models at solar and low metallicities. All necessary `MESA` input files to reproduce our models are available at `https://github.com/niharika-sravan/IIb_progenitors`.

2.2.1. Solar-Metallicity Models

We compute solar-metallicity single-star models with initial mass, $\log_{10}(M_{\rm ZAMS}/M_\odot)$ = 1.3445 – 1.409 ($M_{\rm ZAMS}/M_\odot \simeq 22$ – 26) in intervals of 0.0005 dex. The model with $\log_{10}(M_{\rm ZAMS}/M_\odot) = 1.409$ is the most massive solar-metallicity single-star model that is not stripped before reaching CC (see above for our definitions of stripping and CC).

We compute solar-metallicity binary-star models with initial primary mass, $\log_{10}(M_{\rm ZAMS,1}/M_\odot) = 1.0 - 1.4$ ($M_{\rm ZAMS,1}/M_\odot \simeq 10$ – 25) in intervals of 0.02 dex, initial mass ratio, $q_{\rm ZAMS} \equiv M_{\rm ZAMS,2}/M_{\rm ZAMS,1} = 0.225$ – 0.975 in intervals of 0.05, and initial orbital period, $\log_{10}(P_{\rm orb,ZAMS}/{\rm d}) = 2.5$ – 3.8 ($P_{\rm orb,ZAMS}/{\rm d} \simeq 316$ – 6310) in intervals of 0.02 dex. We only consider case B or later mass transfer (i.e. mass transfer after core hydrogen exhaustion) in this work; a systematic investigation of case A mass transfer (i.e. mass transfer before core hydrogen exhaustion) towards SNe IIb is beyond the scope of this work and would be an interesting line of future investigation. Thus the upper limit on the initial primary mass is set to the mass of the most massive single-star model that is stripped by its own stellar winds ($M_{\rm ZAMS} = 25.6 M_\odot$), since case B or later mass transfer will only result in additional mass loss as the core is already established. We compute the models for $\epsilon = 1.0$ (fully conservative mass transfer), 0.5, 0.1 and 0.01. Models with $\epsilon = 0.5$ and 0.1 are the same as those analyzed in Sravan et al. (2018).

2.2.2. Low-Metallicity Models

We compute a low-metallicity single-star model with initial mass, $\log_{10}(M_{\rm ZAMS}/M_\odot) =$ 1.7 ($M_{\rm ZAMS}/M_\odot \simeq 50$). Models with $\log_{10}(M_{\rm ZAMS}/M_\odot) > 1.7$ take prohibitively long to compute. However, we show in Sections 4.1, 4.2, and 5 that we are still able to draw meaningful conclusions regarding progenitor channels towards SNe IIb at low metallicity.

We compute low-metallicity binary-star models with the same initial primary masses and initial mass ratios as at solar. However, we use coarse (0.1 dex) and fine (0.02 dex) intervals for initial orbital periods below and above $\log_{10}(P_{\rm orb,ZAMS}/{\rm d}) = 2.7$ ($P_{\rm orb,ZAMS} \simeq 501$ days), respectively, to reduce computational demand at short periods while adequately resolving progenitors experiencing late case B and case C (mass transfer after core helium exhaustion) mass transfer at long periods. Once again, our coverage of the range in orbital periods does not capture case A mass transfer. We limit the initial primary mass to $M_{\rm ZAMS,1} \simeq 25 M_{\odot}$, even though our single-star models at low metallicity retain large envelopes at this mass, due to computational reasons. However, we show in Section 5 that potential SN IIb progenitors with $M_{\rm ZAMS,1} \gtrsim 25 M_{\odot}$ are relatively very few and do not affect our inference for progenitor channels significantly. We compute all the aforementioned low-metallicity models for $\epsilon = 0.5$ and 0.1. We do not use $\epsilon = 1.0$ and 0.01, because, as we show in Section 4.1, the parameter spaces at $\epsilon = 0.01$ and 0.1 are quite similar and the parameter space at $\epsilon = 1.0$ is quite small at solar metallicity. In addition, mass transfer is expected to be non-conservative due to rapid spin-up of the secondary to critical rotation during mass transfer (Packet, 1981; Petrovic et al., 2005; Ritchie et al., 2012, also see Popham & Narayan (1991) for a counter argument).

CHAPTER 3

Method to Investigate Type IIb SN Progenitors

3.1. Defining Type IIb SN Progenitors

Models described in Section 2 with primaries that reach CC with residual hydrogen envelope mass[1] $0.01M_{\odot} \leq M_{\mathrm{H\ env,preSN(,1)}} \leq 1M_{\odot}$ are defined as SN IIb progenitors. This is our fiducial definition. The upper limit on the residual hydrogen envelope mass is a generous one since inferred values for it for SNe IIb with detected progenitors are $\lesssim 0.5M_{\odot}$(Woosley et al., 1994; Houck & Fransson, 1996; Bersten et al., 2012; Morales-Garoffolo et al., 2014; Arcavi et al., 2017; Bersten et al., 2018). SNe IIb with detected progenitors have the most massive and thus most extended envelopes (Yoon et al., 2017) among all SN IIb progenitors, as more compact progenitors would be harder to detect. Further, the cooling envelope feature in the SN IIb light curve would be harder to detect for more compact progenitors as it decreases with decreasing envelope radius/mass (Moriya et al., 2016). However, we also apply cuts on the residual hydrogen envelope mass ($0.01M_{\odot} \leq M_{\mathrm{H\ env,preSN(,1)}} \leq 0.5M_{\odot}$) and helium core mass ($2M_{\odot} \leq M_{\mathrm{He\ core,preSN(,1)}} \leq 6M_{\odot}$; Nomoto et al., 1993; Woosley et al., 1994; Morales-Garoffolo et al., 2014; Ergon et al., 2014; Folatelli et al., 2015; Ergon et al., 2015) motivated by values derived for them for SNe IIb with detected progenitors.

[1]The hydrogen envelope-helium core boundary is defined as the outermost point where the hydrogen mass fraction ≤ 0.01 and the helium mass fraction ≥ 0.1.

3.2. Statistical Methods

We assume the following fiducial distributions of binary fraction, ZAMS mass, initial mass ratio, and initial orbital period. We assume the distribution of the fraction of binary systems, $f_{\rm bin}$, is flat with respect to ZAMS mass, initial mass ratio, and initial orbital period. The distribution of initial mass, $M_{\rm ZAMS}$, of all stars is assumed to be the Salpeter IMF (Salpeter, 1955)

$$f(M_{\rm ZAMS}) = (M_{\rm ZAMS})^{-\alpha}. \tag{3.1}$$

We assume that the minimum ZAMS mass to undergo CC is $8M_\odot$ (Woosley et al., 2002; Smartt, 2009). We adopt a power-law distribution for the initial mass ratio, $q_{\rm ZAMS}$,

$$f(q_{\rm ZAMS}) = (q_{\rm ZAMS})^{\beta}. \tag{3.2}$$

We assume that it is valid between $0.2 \leq q_{\rm ZAMS} \leq 1.0$ (Kobulnicky et al., 2014). Finally, we assume a power-law distribution for the initial orbital period, $\log_{10} P_{\rm orb,ZAMS}$,

$$f(\log_{10} P_{\rm orb,ZAMS}) = (\log_{10} P_{\rm orb,ZAMS})^{\gamma}. \tag{3.3}$$

We assume that it is valid $0.15 \leq \log_{10}(P_{\rm orb,ZAMS}/{\rm d}) \leq 3.80$ (the upper limit on the initial orbital period modeled in this work). Note that while massive binary properties are observed to be relatively insensitive to metallicity only between solar and Large Magellanic Cloud metallicities (and initial orbital periods from 1–1000 days; Almeida et al., 2017), we assume that they are preserved down to a fourth-solar.

We use several values of $f_{\rm bin}$, α, β, and γ. For $f_{\rm bin}$ we use 0.25, 0.5, 0.65, and 0.8. The first two are to allow comparison of our results against those of Claeys et al. (2011), while the last two are the upper and lower limits on $f_{\rm bin}$ found by Kobulnicky et al. (2014). For α we use 1.6, 2.3, 3.0 to capture the range in alpha (Kroupa, 2001; Schneider et al., 2018). For β we use -1.0 (negative values of β favor binaries with low $q_{\rm ZAMS}$ or unequal binary component masses) and 0.0. $\beta = 0.0$ is according Kobulnicky et al. (2014) and $\beta = -1.0$ is to allow comparison of our results against those of Claeys et al. (2011). For γ we use 0.0 and -0.22. The first is Öpik's law (Öpik, 1924), while the second is according Kobulnicky et al. (2014). Note that, though the distribution of Kobulnicky et al. (2014) is only valid up to $P_{\rm orb,ZAMS} = 2000$ days, we assume that it holds up to $\simeq$ 6310 days. However, we note that we find good agreement with SN IIb rates computed using the distributions of Moe & Di Stefano (2017, discussed next) that are valid for larger values of $P_{\rm orb,ZAMS}$. We adopt $f_{\rm bin} = 0.5$, $\alpha = 2.3$, $\beta =$ -1, and $\gamma = -0.22$ as our fiducial values.

In addition to the simple distributions discussed above, we also consider recent distributions derived by Moe & Di Stefano (2017) to calculate SN IIb rates. We simulate a large population (10^6 samples) of single and binary stars with initial (in binary systems, primary) mass $M_{\rm ZAMS} \geq 8M_\odot$ using a Monte Carlo technique and use the simulated population to compute rates. For this assume the Salpeter IMF and $\alpha = 1.6$, 2.3, and 3.0.

Finally, we assume that each model with initial parameters, $\vec{\theta}_{\rm mod}$ (i.e. $M_{\rm ZAMS}$ and, in binaries, $q_{\rm ZAMS}$ and $P_{\rm orb,ZAMS}$), are representative of all models with initial parameters $\in [\vec{\theta}_{\rm mod} - \Delta\vec{\theta}_{\rm mod}/2, \vec{\theta}_{\rm mod} + \Delta\vec{\theta}_{\rm mod}/2]$, where $\Delta\vec{\theta}_{\rm mod}$ is vector of parameter spacing. If the parameter space spacing changes at a given initial parameter, $\hat{\theta}_{\rm mod}$ (which is the case for $\log_{10}(P_{\rm orb,ZAMS}/{\rm d})$=2.7 in low-metallicity models), we assume that these models are representative of all models with initial parameters $\in [\hat{\theta}_{\rm mod} - \Delta\hat{\theta}_{{\rm mod},<}/2, \hat{\theta}_{\rm mod} + \Delta\hat{\theta}_{{\rm mod},>}/2]$ where $\Delta\hat{\theta}_{{\rm mod},<}$ and $\Delta\hat{\theta}_{{\rm mod},>}$ are the parameter spacings below and above $\hat{\theta}_{\rm mod}$, respectively.

CHAPTER 4

Evolutionary Pathways Towards Type IIb SNe

4.1. Parameter Space of Type IIb SNe

We use models described in Section 2, method described in Section 3, and fiducial values of $f_{\rm bin}$ (0.5), α (2.3), β (-1.0), and γ (-0.22) to examine the parameter space for single- and binary-star SN IIb progenitors at solar and low metallicities.

All solar- and low-metallicity single-star models described in Sections 2.2.1 and 2.2.2 and listed in Table 2.1 are SN IIb progenitors using our fiducial definition. However, because $M_{\rm He\ core,preSN(,1)} = 26 M_\odot$ for our least massive low-metallicity model ($M_{\rm ZAMS}/M_\odot \simeq 50$), we do not expect that these and more massive models won't explode as SNe and instead collapse directly into black holes (Fryer, 1999). Using the tighter cut $0.01 M_\odot \leq M_{\rm H\ env,preSN(,1)} \leq 0.5 M_\odot$ models with $M_{\rm ZAMS} \simeq 23 - 25.5\ M_\odot$ at solar metallicity are SN IIb progenitors. However, because we only compute low-metallicity single-star models up to $M_{\rm ZAMS} \simeq 50\ M_\odot$ (which is the least massive SN IIb progenitor using our fiducial definition; see Section 2), we are unable to delineate corresponding parameter space at low metallicity using this cut. On the other hand, applying the $2 M_\odot \leq M_{\rm He\ core,preSN(,1)} \leq 6 M_\odot$ cut qualifies no single stars, either at solar or low metallicity, as SN IIb progenitors: $M_{\rm He\ core,preSN(,1)} = 9.5\ (26) M_\odot$ for the least massive SN IIb progenitor (using our fiducial definition) at solar (low) metallicity.

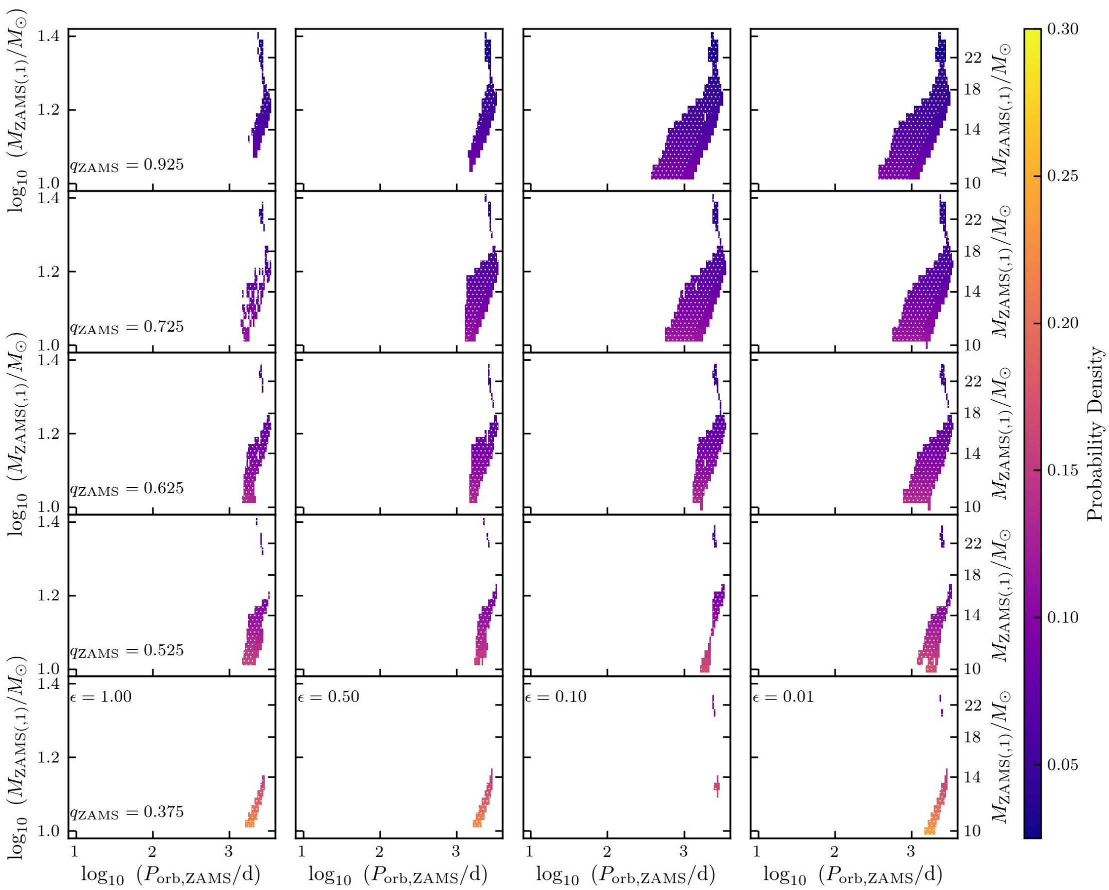

Figure 4.1 Parameter space for binary SN IIb progenitors at solar metallicity. Horizontal panels show models with representative $q_{\rm ZAMS} \equiv M_{\rm ZAMS,2}/M_{\rm ZAMS,1}$ (noted to the bottom-left in the left-most panels) demonstrating how the parameter space changes with $q_{\rm ZAMS}$. Vertical panels from left to right show models with mass transfer efficiency, $\epsilon = 1.0$ (fully conservative mass transfer), 0.5, 0.1 and 0.01. The color scale shows the probability density using our fiducial distributions for initial properties of binary stars (see Section 3). The dotted regions show the parameter sub-space using the criterion $0.01 M_\odot \le M_{\rm H\ env,preSN(,1)} \le 0.5 M_\odot$ to define SN IIb progenitors. The parameter space decreases with $q_{\rm ZAMS}$ and decreases more with decreasing ϵ as discussed in Section 4.2.

Figures 4.1 and 4.2 show the parameter space for binary SN IIb progenitors (using our fiducial definition) at solar and low metallicity, respectively. The parameter space

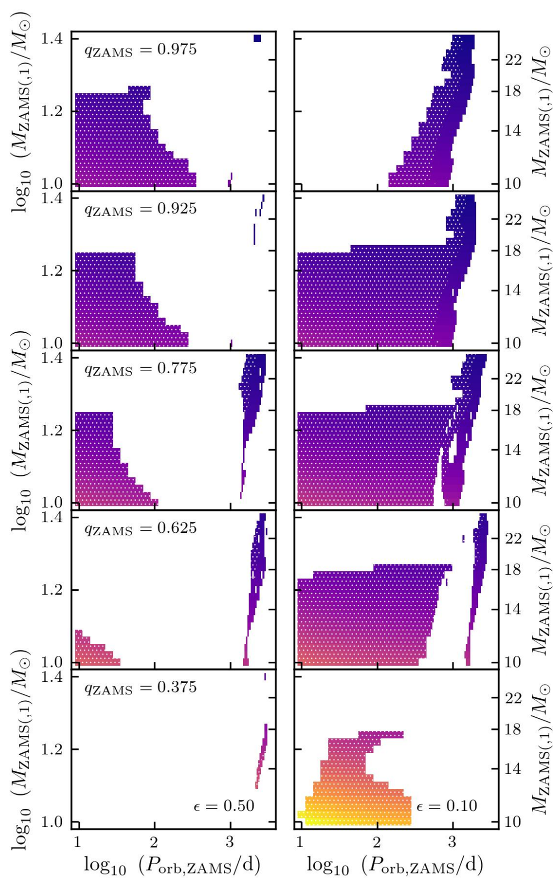

Figure 4.2 Parameter space for binary SN IIb progenitors at low metallicity. Horizontal panels show models with representative q_{ZAMS} (noted to the top-left in the left-most panels) demonstrating how the parameter space changes with q_{ZAMS}. Left and right vertical panels show models with mass transfer efficiency, $\epsilon = 0.5$ and 0.1, respectively. The color scale and dotted regions have the same meaning as in Figure 4.1. The gap in the parameter space between $\log_{10}(P_{orb,ZAMS}/d) \simeq 1.5(2) - 3$ when ϵ = 0.5 is due to occurrence of contact in the binaries (described in Section 4.2). The presence of SN IIb progenitors with short initial orbital periods and $q_{ZAMS} = 0.975$ when $\epsilon = 0.5$ is due to rejuvenation in secondaries (see Section 4.2).

increases dramatically with decreasing metallicity. This is because of difference in models that initiate mass transfer on the Hertzsprung Gap (HG). After the mass transfer phase, primary stars at both metallicities detach with small amounts of residual hydrogen envelopes, with those at lower metallicities retaining more massive envelopes (Götberg et al., 2017). During the core helium burning phase, strong winds at solar metallicity successfully strip the primary. However, at low metallicities, winds are too weak to complete the stripping and the primary stars explode as SNe IIb. This was also shown by Yoon et al. (2017) who found that decreasing mass-loss rates gives roughly analogous results to those from decreasing metallicity. Because of the large change in primary radius that occurs when crossing the HG, the range of initial orbital periods that permit mass transfer during this phase is very broad.

The parameter space decreases with increasing ϵ at both metallicities. This is because of increasing likelihood of contact in the binaries when the secondary is unable to thermally relax with its acquired mass at higher ϵ (Braun & Langer, 1995). The parameter space at solar metallicity and when $\epsilon = 0.1$ and 0.01 is quite similar.

The parameter space generally decreases with $q_{\rm ZAMS}$ due to increasing liklihood of contact in the binaries. By extension, the parameter space decreases more with $q_{\rm ZAMS}$ at lower ϵ, as more material leaving the system carrying its orbital momentum causes the orbit to shrink faster, promoting conditions for the development of contact or unstable mass transfer (see Section 4.2 and Figure 4.4 for details).

The parameter space with $q_{\rm ZAMS} \lesssim 0.4$ is almost entirely progenitors with $M_{\rm H\ env,preSN(,1)} \leq 0.5 M_{\odot}$ at both metallicities. Applying the cut $2M_{\odot} \leq M_{\rm He\ core,preSN(,1)} \leq 6M_{\odot}$, effectively excludes the parameter space above $M_{\rm ZAMS,1} \simeq 16\ M_{\odot}$ at both metallicities. This is because the core is already established before the onset of interaction in the binary-star models considered in this work (see Section 2.2.1).

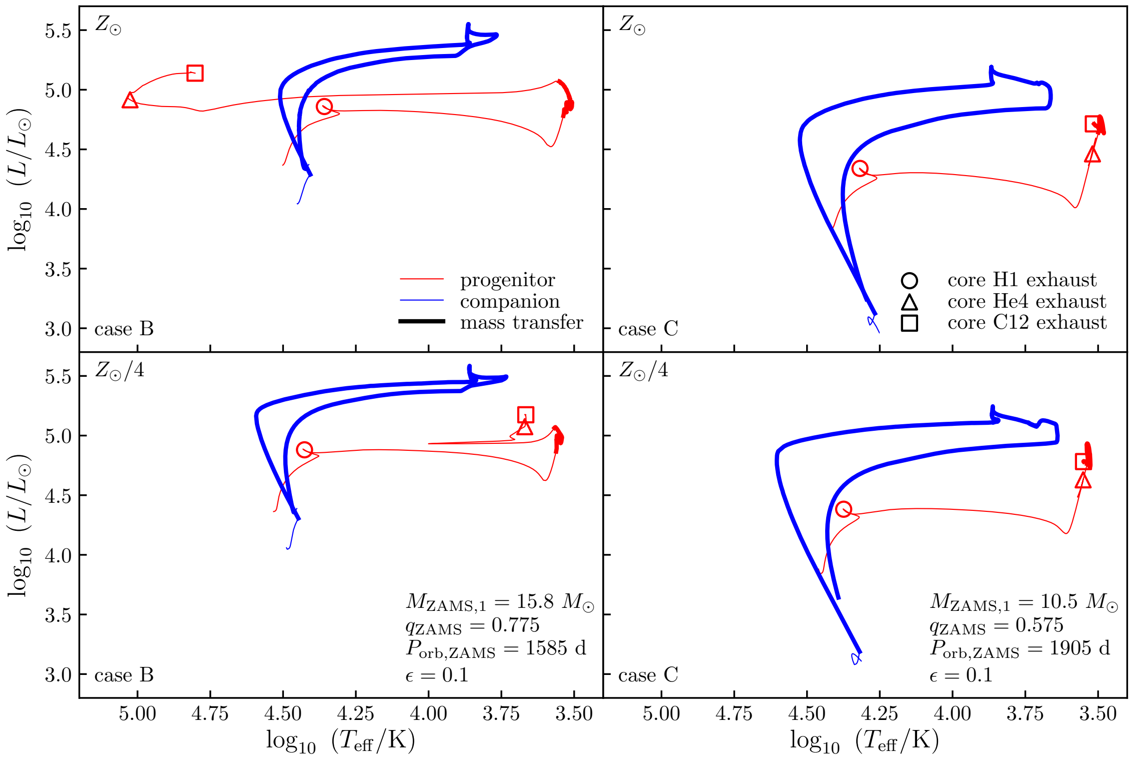

Figure 4.3 Hertzsprung-Russell (H-R) diagrams showing typical evolutionary pathways to binary (red: primary and blue: secondary) SN IIb progenitors at solar (top panels) and low (bottom panels) metallicities. Mass transfer (shown using thicker lines) is defined to be taking place when mass transfer rate due to RLO is $\geq 10^{-6} M_\odot$ yr^{-1}. Circles, triangles, and squares denote points when H1, He4, and C12 (according to definitions in Sections 2) is exhausted in the center of the corresponding binary component, respectively. Left panels show typical evolution via case B mass transfer (mass transfer after core hydrogen exhaustion but before core helium exhaustion). Right panels show typical evolution via case C mass transfer (mass transfer after core helium exhaustion).

4.2. Evolutionary Channels

4.2.1. Solar Metallicity

Top panels of Figure 4.3 show typical evolutionary pathways via case B and C mass transfer to SNe IIb at solar metallicity. Case C mass transfer for SNe IIb is important

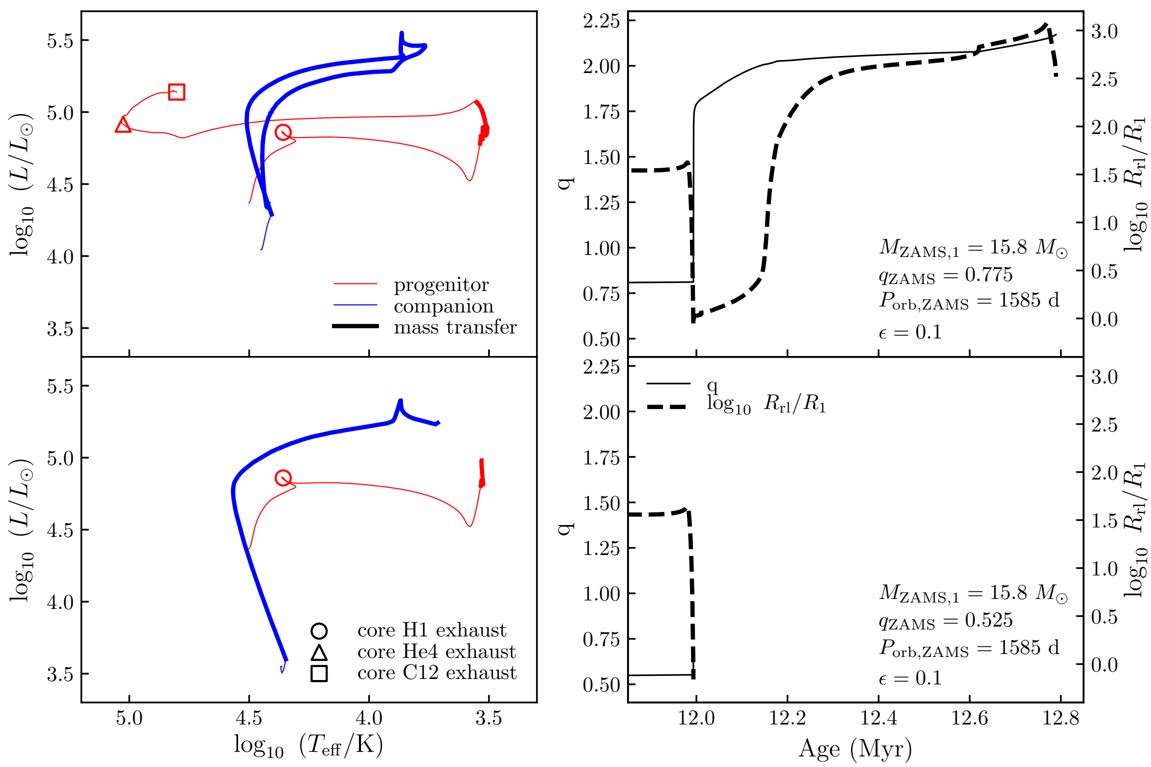

Figure 4.4 *Left*: H-R diagrams showing evolution of solar-metallicity binary-star models that avoid (top) or enter (bottom) contact due to difference in $q_{\rm ZAMS}$. Line colors, line weights, and symbols have the same meaning as in Figure 4.3. *Right*: Evolution of mass ratio $q \equiv M_2/M_1$ (solid line) and fraction of Roche-lobe to primary radius (dashed line) as a function of binary age for the corresponding models on the left. After the onset of mass transfer at $\sim$ 12 Myr, change in q in the model with higher $q_{\rm ZAMS}$ is enough to cause the orbit to expand (increasing Roche-lobe radius) in response to further mass transfer, slowing it down.

for lower primary masses as these expand significantly after core helium exhaustion. However, this channel is only possible for a narrow range in initial orbital periods that shrinks with increasing primary mass.

The viability of both channels mentioned above depends on the initial mass ratio and the efficiency of mass transfer in the binary. If after initiating mass transfer the mass ratio remains low enough that the orbit continues to shrink as a response

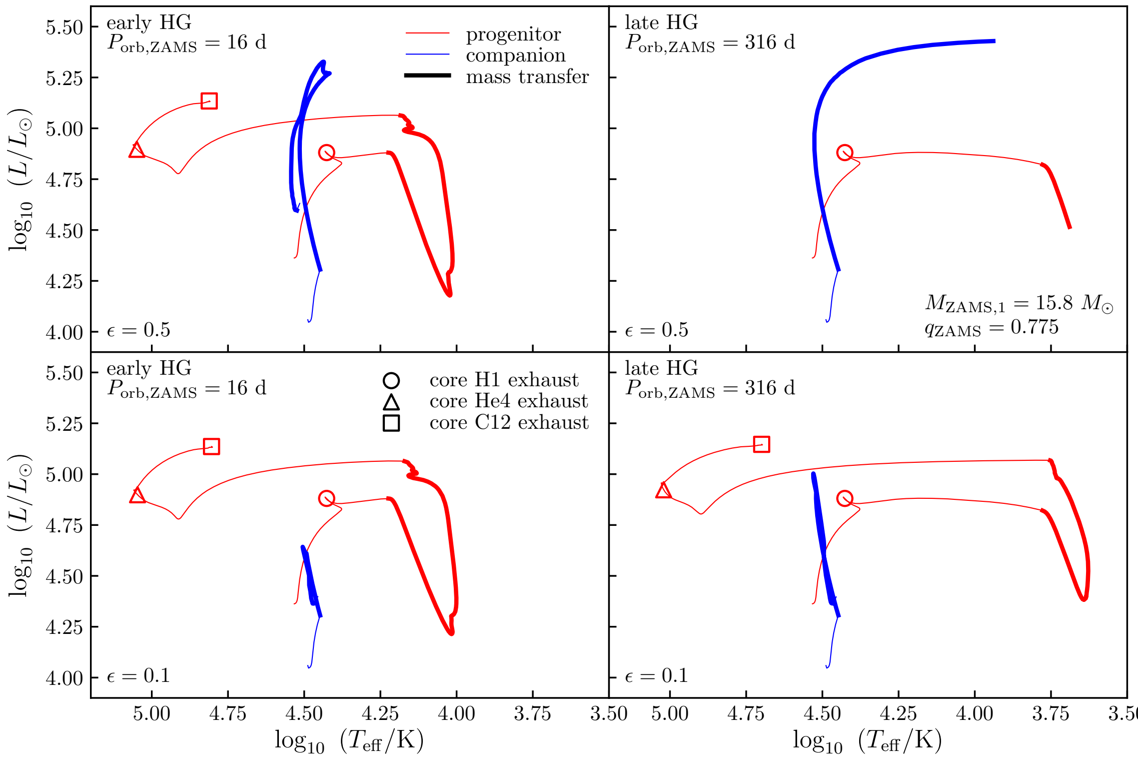

Figure 4.5 H-R diagrams showing evolution of low-metallicity binary-star models that initiate mass transfer early (left) or late (right) on the HG. Line colors, line weights, and symbols have the same meaning as in Figure 4.3. Only the model on the top-right enters contact.

to further mass transfer, contact will ensue. This is more likely for binaries with lower initial mass ratios and ϵ (more material leaving the system carries its orbital momentum, shrinking the orbit). This is demonstrated in Figure 4.4. As pointed out in Section 4.1, this phenomenon results in the SN IIb parameter space decreasing with $q_{\rm ZAMS}$ and decreasing more at lower ϵ. Similarly, binary-star models with high ϵ (but similar $q_{\rm ZAMS}$) are more likely to end up in contact when the secondary is unable to thermally relax as it acquires mass. As pointed out in Section 4.1, this phenomenon results in the SN IIb parameter space decreasing with ϵ (at similar $q_{\rm ZAMS}$).

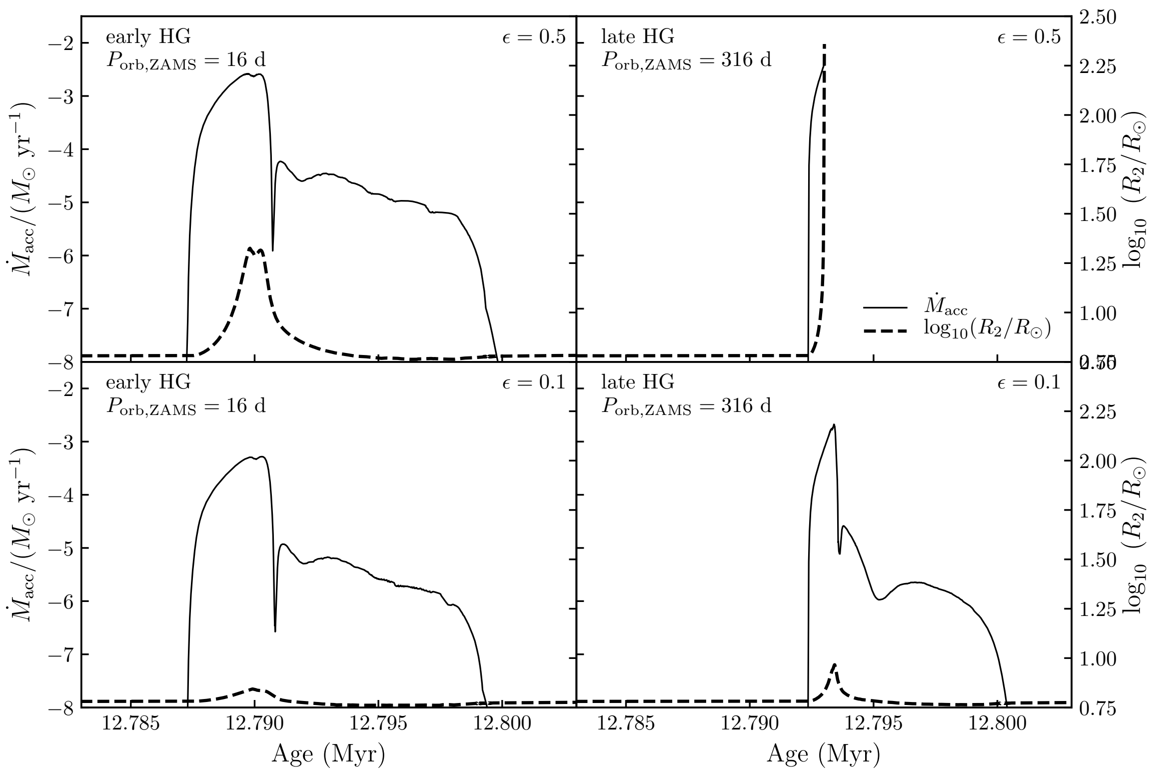

Figure 4.6 Mass accretion rate (solid line) and radius (dashed line) as a function of age of the secondary for the corresponding models in Figure 4.5. In these models, mass transfer occurs on the thermal timescale of the primary (and proportional to the primary radius). When higher mass transfer rates (for larger primary radii later on the HG) are compounded by higher accretion efficiencies, the secondary approaches a limit, acquiring mass significantly faster than its thermal timescale. This results in its radius increasing dramatically, as in the top-right model, and the binary entering contact.

4.2.2. Low Metallicity

Bottom panels of Figures 4.3 and 4.5 show typical evolutionary pathways via case B and C mass transfer to SNe IIb at low metallicity. Properties of case C mass transfer are similar to those at solar metallicity. However, there is a drastic difference in the channels available via case B mass transfer. While the pathways via mass transfer starting when the primary is ascending on the giant branch remains similar at both

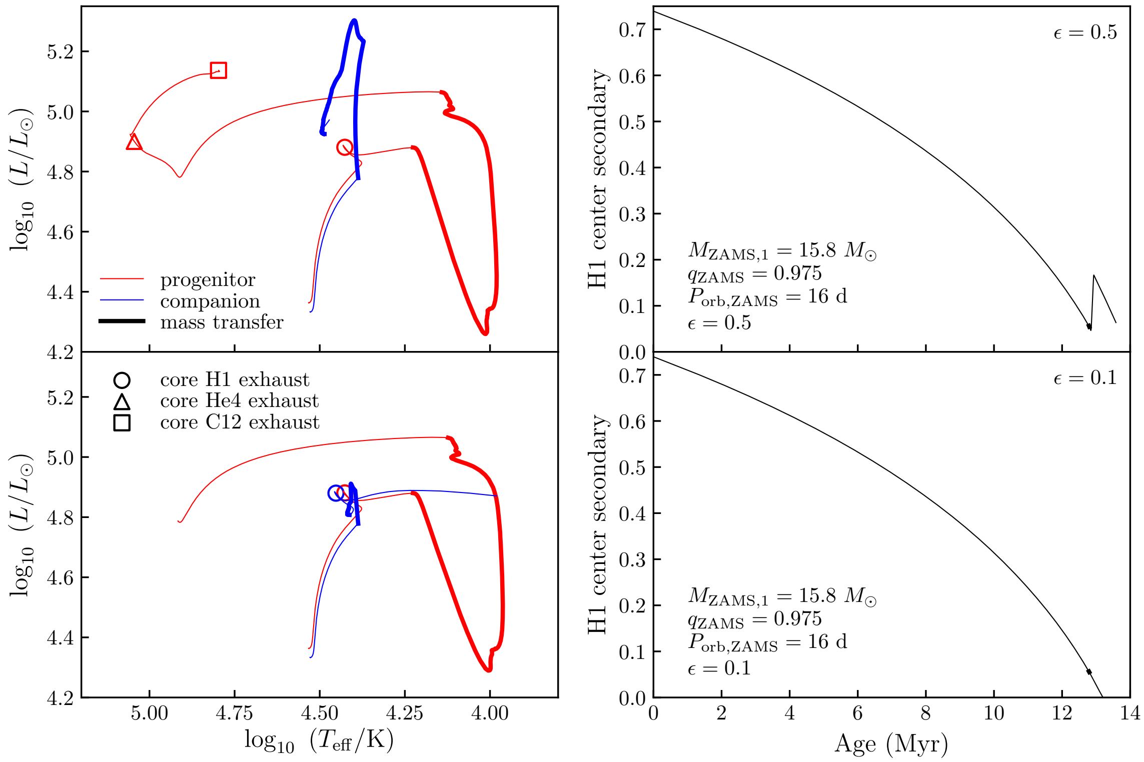

Figure 4.7 *Left*: H-R diagrams showing evolution of low-metallicity binary-star models with high mass ratios and $\epsilon = 0.5$ (top) and $\epsilon = 0.1$ (bottom). Line colors, line weights, and symbols have the same meaning as in Figure 4.3. *Right*: Evolution of central hydrogen mass fraction in the secondary as a function of binary age for the corresponding models on the left. The secondary in the model with $\epsilon = 0.1$ acquires very little mass during mass transfer, exhausts hydrogen in its center, expands as it leaves the main-sequence and enters contact. However, the secondary in the model with $\epsilon = 0.5$ acquires enough mass to rejuvenate, allowing the primary to evolve to CC.

solar and low metallicites, there are additional pathways available at low metallicity when the primary initiates mass transfer when crossing the HG. This is discussed in detail in Section 4.1 and is primarily a consequence of the scaling in wind mass-loss rates with metallicity.

As is for solar metallicity, the viability of all above mentioned channels depends on the initial mass ratio and the efficiency of mass transfer in the binary, decreasing with decreasing $q_{\rm ZAMS}$ and increasing ϵ as described above. However, the latter has a much more dramatic effect at low metallicity for binary-star models that initiate mass transfer when the primary is crossing the HG. Figures 4.5 and 4.6 show the difference in evolution when mass transfer begins late on the HG for different ϵ. When the primary initiates mass transfer on the HG it transfers mass on its thermal timescale , which is shorter later on the HG or for larger radii (Wellstein et al., 2001). If the mass transfer efficiency is high enough that accretion occurs significantly faster than the thermal timescale of the secondary then the binary will enter contact.

At very high initial mass ratio ($q_{\rm ZAMS} = 0.975$) at low metallicity there are a couple of interesting deviations from the standard channels described above. First, as can be seen from Figures 4.1 and 4.2, majority of case B and C SN IIb progenitors with high initial mass ratios and $\epsilon = 0.5$ expected at low metallicity from solar-metallicity models enter contact. Second, there is an absence of SN IIb progenitors with short orbital periods and $q_{\rm ZAMS} = 0.975$ at $\epsilon = 0.1$. Figure 4.7 shows the evolution of two binary-star models with $q_{\rm ZAMS} = 0.975$ and different ϵ. Initially, both secondaries have similar evolutionary timescales to their primaries. In the model with $\epsilon = 0.1$, the secondary accretes relatively small amounts of mass (keeping it essentially undisturbed) and quickly follows the primary in its evolution: exhausting hydrogen in its center, expanding as it leaves the main-sequence, and entering contact. However, in the model with $\epsilon = 0.5$, the secondary accretes enough mass to rejuvenate, allowing the primary to evolve to CC before the secondary leaves the main-sequence.

4.3. Key Takeaways

We find that the parameter space for single-star SN IIb progenitors decreases and that for binary-star SN IIb progenitors increases with decreasing metallicity. This difference is a consequence of the scaling in stellar winds with metallicity. We also find that the parameter space of SNe IIb increases with decreasing efficiency of mass transfer.

CHAPTER 5

Rates of Type IIb SNe

We use models described in Section 2 and method described in Section 3 to compute SN IIb rates at solar and low metallicities. We assume that all secondaries explode as SNe and that none of them are of Type IIb. These assumptions are likely true for majority of the secondaries considered in this work. Possible exceptions include (1) secondaries with ZAMS masses $\lesssim 8M_{\odot}$ that do not accrete much mass, (2) solar-metallicity secondaries with ZAMS masses $\simeq 23-26M_{\odot}$ that are mostly undisturbed (see Section 4.1), i.e. accrete or lose very little mass due to binary interactions (even after the primary star explodes as a SN), and (3) secondaries with ZAMS masses $\simeq 8-23M_{\odot}$ that undergo significant mass loss due to binary interactions after the primary star explodes. The assumptions yield a lower limit on the estimate for SN IIb rates. Conversely, the upper limit, assuming that none of the secondaries explode as SNe, can be obtained by multiplying the lower limit by $(1+f_{\rm bin})$. Since we only have a lower limit on the single-star ZAMS mass at low metallicity that is a SN IIb using our fiducial definition, we assume that the mass range for single-star low-metallicity SN IIb progenitors is the same as that at solar (0.0645 dex). For the same reason we are unable to delineate the parameter space for single-star SNe IIb at low metallicity using only the cut $0.01M_{\odot} \leq M_{\rm H\ env,preSN(,1)} \leq 0.5M_{\odot}$.

5.1. Rates

Tables A.1 and A.2 list single- and binary-star (with $\epsilon = 0.5$ and 0.1) SN IIb rates at solar and low metallicity, respectively, for all values for $f_{\rm bin}$, α, β, and γ and all four definitions for SN IIb progenitors outlined in Section 3. Similarly, Table A.1 lists single- and binary-star (with $\epsilon = 0.5$ and 0.1) SN IIb rates at solar and low metallicity, computed using the distributions of Moe & Di Stefano (2017) and method described in Section 3, for all values for α and all four definitions for SN IIb progenitors. For these we provide the lower and upper limits on the rates, assuming that all or none of the secondaries explode as SNe, respectively. The rates are typically 2-5 times lower than those from our fiducial priors (applying $f_{\rm bin} = 0.88$; value for the simulated population using the distributions of Moe & Di Stefano (2017)).

Our SN IIb rates are consistent with the results of Claeys et al. (2011): for $\epsilon = 0.5$, $f_{\rm bin} = 0.5$, $\beta = 0.0$, and $\gamma = 0.0$, we compute a binary-star SN IIb rate of $0.35-0.55\%$, while Claeys et al. (2011) estimated 0.7%. The rates increase by $< 0.01\%$ when we require that primary stars transfer at least 0.1% (instead of 1% in our fiducial assumption) of their initial mass in RLO. The low-metallicity rates are more strongly robust to this definition; there are relatively few mildly interacting binaries at low metallicity. As mentioned in Section 2.2.2, we limit the initial primary mass to $M_{\rm ZAMS,1} \simeq 25 M_\odot$ in our low-metallicity models even though the corresponding single-star models retain large envelopes. We find that 'potential' low-metallicity SN IIb progenitors with $M_{\rm ZAMS,1} \gtrsim 25 M_\odot$ ($q_{\rm ZAMS} = 0.4 - 1.0$ and $\log_{10}(P_{\rm orb,ZAMS}/{\rm d}) = 3.0 - 3.7$) contribute at most $< 1\%$ in rates.

Table 5.1. Theoretical versus observationally inferred SN IIb rates

	Theoretical (this work)			Observational
metallicity	single	binary	single+binary	
high ($Z_{\odot}$)	$0 - 3.5$	$0 - 2$	$0 - 4.5$	$10 - 12$ [a,b,c]
low ($Z_{\odot}/4$)	$0 - 1.5$	$0.5 - 14$	$0.5 - 15$	20 [c,d]

Note. — SN IIb rate is defined as fraction of SNe IIb vs all CC SNe percent.

References. — [a] Li et al. (2011); [b] Smith et al. (2011); [c] Graur et al. (2017); [d] Arcavi et al. (2010)

Table 5.1 summarizes our results for SNe IIb rates. The upper limit on the single (binary) SN IIb rate corresponds to those from favorable priors [$f_{\rm bin}$ = 0.25 (0.8), α = 2.3], assuming that none of the secondaries explode as SNe, and, at low metallicity, adding 'potential' progenitors with $M_{\rm ZAMS,1} \gtrsim 25 M_{\odot}$. The upper limit on the total solar (low) metallicity SN IIb rate corresponds to those from favorable priors [$f_{\rm bin}$ = 0.25 (0.8), α = 2.3], assuming that none of the secondaries explode as SNe, and, at low metallicity, adding 'potential' progenitors with $M_{\rm ZAMS,1} \gtrsim 25 M_{\odot}$. We note that our binary SN IIb rates at low metallicity represent lower limits as we do not compute progenitors arising via case A mass transfer. We do not expect SN IIb progenitors arising via case A mass transfer at solar metallicity because the residual hydrogen envelope after the mass transfer phase will be roughly as massive as that for binary stars that initiate mass transfer on the HG (Götberg et al., 2017) and will therefore also be stripped before CC.

Overall, our model (single and binary) SNe IIb contribute to $0-4.5\%$ and $0.5-15\%$ of all CC SNe at solar and low metallicity, respectively. SN IIb rates from observations is 10−12% (Li et al., 2011; Smith et al., 2011; Shivvers et al., 2017) at high metallicity. Therefore, our models can account for less than half the observationally inferred rate at high metallicity. On the other hand, there is evidence that SN IIb rates may be higher in lower than LMC-mass galaxies (Arcavi et al., 2010; Graur et al., 2017). Note that observationally inferred rates as a function of galaxy mass/metallicity should be interpreted with caution as they are affected by small sample sizes. However, if this trend holds up in future investigations using large sample sizes, our models can account for most of the implied SNe IIb rates at low metallicity ($\sim$ 20%, Arcavi et al., 2010; Graur et al., 2017).

5.2. Implications

Binary interactions and their high incidence are generally cited to resolve the high observed fraction of SNe IIb. However, we find that single and binary stars contribute roughly the same (singles slightly more) to SNe IIb at solar metallicity. Binary stars only dominate as SN IIb progenitors at low metallicity. In addition, at high metallicity, neither single nor binary stars nor both can account for the observed fraction of SNe IIb. Our models are only able to account for SNe IIb rates currently indicated by observations at low metallicity. We note that the above issues are exacerbated when we apply more restrictive definitions for SNe IIb progenitors as indicated from analysis of individual events (e.g. residual hydrogen envelope and helium core mass).

These results have the following implications for progenitor channels to SNe IIb:

(1) At solar metallicity, the wind mass-loss rate needs to be lower than those used in our models.

(2) We require low mass transfer efficiencies to explain observed SN IIb rates: solar (low) metallicity binary-star SNe IIb with $\epsilon = 0.5$ contribute to $<1\%$ (5%) of CC SNe.

CHAPTER 6

Observable Properties of Type IIb SN Progenitors

We use models described in Section 2 and method described in Section 3 to derive distributions of single and binary SN IIb progenitor properties of our models at solar and low metallicities that can also be constrained observationally using LCs, direct detection of progenitors, and observations in X-rays and radio wavelengths. The goal is to compare theoretically predicted to observationally constrained properties of SNe IIb to identify channels that are represented in observations and also identify additional or missing channels indicated by theory or observations, respectively. In this work, whenever observationally derived values have associated uncertainties and we aim to compare to a 'range' in observationally constrained values, we use the $3-\sigma$ range to be conservative.

6.1. Properties from Light Curves

Figure 6.1 shows distributions of single and binary SN IIb progenitor properties at solar and low metallicity that can be constrained using LCs: hydrogen envelope mass, helium core mass, and radius. The distribution of helium core mass and radius of binary SN IIb progenitors at solar metallicity is bimodal.

The high (low) helium core mass peak is due to progenitors with $M_{\rm ZAMS,1} \gtrsim (\lesssim) 20 M_{\odot}$. The high core mass group consists of mildly interacting binaries whose evolution is largely similar to their single-star counterparts. Observations constrain

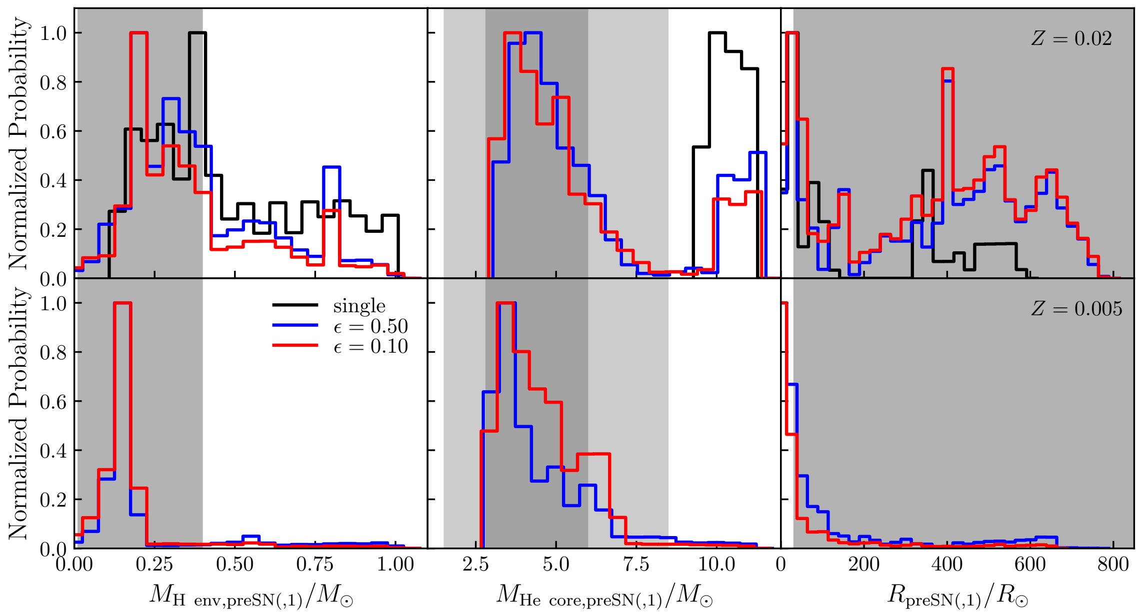

Figure 6.1 Distributions of pre-SN progenitor hydrogen envelope mass ($M_{\mathrm{H\ env,preSN(,1)}}$, left), helium core mass ($M_{\mathrm{He\ core,preSN(,1)}}$, middle), and radius ($R_{\mathrm{preSN(,1)}}$, right) for single (black) and binary ($\epsilon = 0.1$ (red) and 0.5 (blue)) SN IIb progenitors at solar (top) and low metallicity (bottom). Dark shaded regions indicate the range of values derived for SNe IIb with detected progenitors ($M_{\mathrm{H\ env,preSN(,1)}}$ from Arcavi et al. (2017); Bersten et al. (2018), $M_{\mathrm{He\ core,preSN(,1)}}$ from Woosley et al. (1994); Nomoto et al. (1993), $R_{\mathrm{preSN(,1)}}$ from Woosley et al. (1994); Folatelli et al. (2015). Light shaded regions indicate range of SNe IIb progenitor masses calculated by adding $\sim 1.5 M_\odot$ for a neutron star remnant to ejecta masses derived by Lyman et al. (2016). Binary SN IIb progenitors at low metallicity have smaller hydrogen envelope masses and radii than at solar metallicity.

helium core masses of SNe IIb to be between ~ 2 and $9 M_\odot$. This excludes single stars and the binary high core mass group at solar metallicity as SNe IIb progenitors. This result has been underscored extensively in the literature and has been used as one of the key pieces of evidence to support binaries as predominant progenitors of SNe IIb. Interestingly, the low helium core mass peak is similar at both metallicities.

The low (high) radius peak is due to progenitors with $T_{\rm eff} > (<) 10^4$K. Binary SN IIb progenitors at low metallicity have smaller hydrogen envelope masses and radii than at solar metallicity (a peak in progenitor envelope mass translates to a peak in radius, and vice versa; see Section 7). This is because of progenitors with $\log_{10}(P_{\rm orb,ZAMS}/{\rm d}) \lesssim 2.8$ that initiate MT on the Hertzsprung Gap (HG). This channel towards SNe IIb is only viable at low metallicity, where weak winds permit the progenitor to retain its hydrogen envelope left over after the MT phase. As these progenitors experience MT earlier than those with larger initial orbital periods, wind mass loss during their longer remaining lifetime leaves them with a small hydrogen envelope. Since these binaries are favored due to the prior on initial orbital period, this group produces a large peak in the distribution of hydrogen envelope mass.

Observations indicate a broad range for SN IIb progenitor radii and as such do not provide strong constraints. However, the range of radii allowed at solar metallicity is larger. While compact progenitors are excluded by observations, this could be a result of observation bias. Note also that SNe IIb from compact progenitors would be harder to detect because the cooling envelope feature in their LCs would be less pronounced (Moriya et al., 2016). The existence of compact progenitors is supported theoretically and, if present, would favor the presence of weak stellar winds as discussed above.

6.2. Properties from Detection of Progenitors and their Companions

Figure 6.1 shows distributions in the Hertzsprung-Russell (H-R) diagram of single and binary SN IIb progenitors at solar and low metallicity.

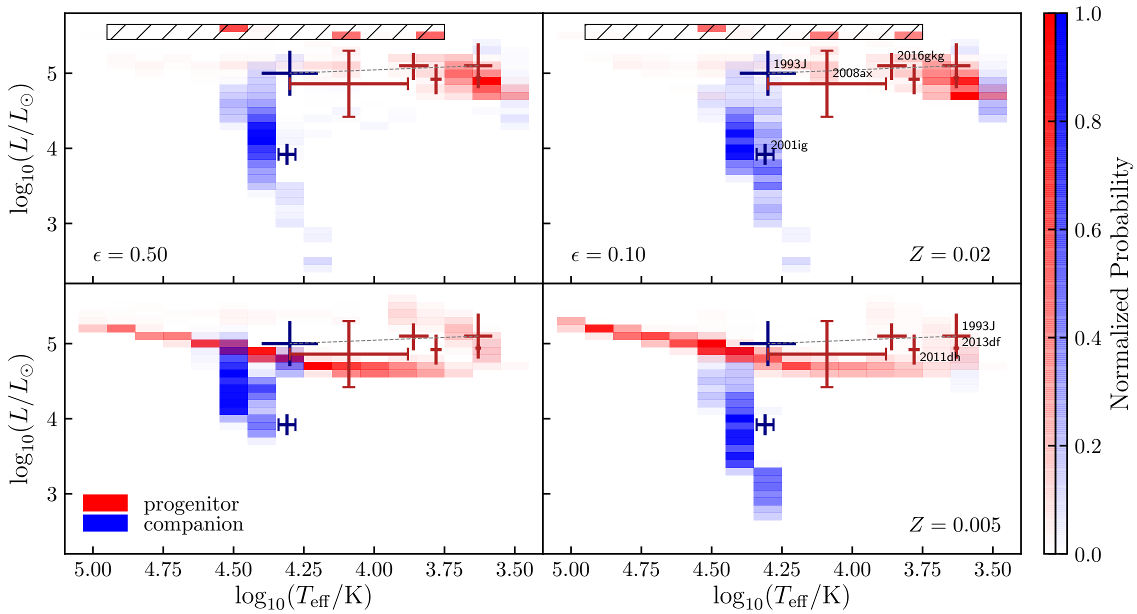

Figure 6.2 Distributions of H-R locations of single and binary ($\epsilon = 0.1$ (right) and 0.5 (left)) SN IIb progenitors at solar (top) and low metallicity (bottom). Red (blue) color scales show normalized probability of binary SN IIb progenitor and companion (secondary) H-R locations. The black hatched region shows the region spanned by single SN IIb progenitors with normalized posterior probabilities ≥ 0.01. Red cross-hairs show H-R locations of progenitors of SNe 1993J (Maund et al., 2004), SN 2008ax (Folatelli et al., 2015), 2011dh (Maund et al., 2011), 2013df (Van Dyk et al., 2014), and 2016gkg (Bersten et al., 2018). Blue cross-hairs show H-R locations of the companions of SNe 1993J and 2008ax (Maund et al., 2004; Ryder et al., 2018b). Cross-hairs without caps indicate $1-\sigma$ ranges whereas those with caps indicate hard limits. The two groups in the progenitor H-R space at low metallicity arise due to difference: the top-right (bottom-left) branch arises from binaries with $\log_{10}(P_{\rm orb,ZAMS}/{\rm d}) \gtrsim (\lesssim) 2.8$ that initiate mass transfer when the primary is on the HG (GB). H-R locations of detected progenitors for SNe IIb are favored at solar metallicity and low mass transfer efficiency ($\epsilon = 0.1$) at low metallicity.

At low metallicity, blue SN IIb progenitors are more likely. This is a result of more compact progenitors at low metallicity (see discussions in Sections 6.1 and 7). Red (evolved) companions are less likely in binaries with $\epsilon = 0.5$ at low metallicity because majority of case B and C progenitors with high initial mass ratios, that would result in such companions, enter contact. Also, the range in companion luminosities for binary SN IIb with $\epsilon = 0.5$ at low metallicity is restricted.

There are two branches in the progenitor H-R space at low metallicity. The top-right branch is similar to the progenitors at solar metallicity. The bottom-left branch, spanning across the H-R diagram, is found almost exclusively at low metallicity. This branch arises from binaries with that initiate mass transfer when the primary is on the HG. As discussed in the previous section, this channel is only permitted at low metallicity and results in compact progenitors with a small hydrogen envelope. As these progenitors are highly stripped they lie along the helium MS (Köhler et al., 2015). Although, the H-R locations of these progenitors are not represented in observations, it may be due to observational bias towards detecting redder stars. However, their existence is supported theoretically, and if detected, would indicate weak stellar winds. Moreover, since they lie along the helium MS, their luminosities can be used to place constraints on their effective temperatures.

H-R locations of detected progenitors of SNe IIb are favored at solar metallicity and low mass transfer efficiency ($\epsilon = 0.1$) at low metallicity. There is a gap in H-R locations of low metallicity SN IIb progenitors with $\epsilon = 0.5$ between the two branches mentioned earlier. This is because progenitors with $\epsilon = 0.5$ that initiate MT late on the HG enter contact. Overall, our binary SN IIb models are able to explain the H-R properties of SN IIb progenitors and companions detected to date. Single SN IIb progenitor H-R properties are excluded within $1-\sigma$ of observed constraints. Our models support the existence of blue ($T_{\rm eff,preSN(,1)} \lesssim 10^5$K) with $\sim 10^{4.5} - 10^{5.5}$ $L_\odot$ progenitors. If present, they would favor weak stellar winds. Our models also indicate

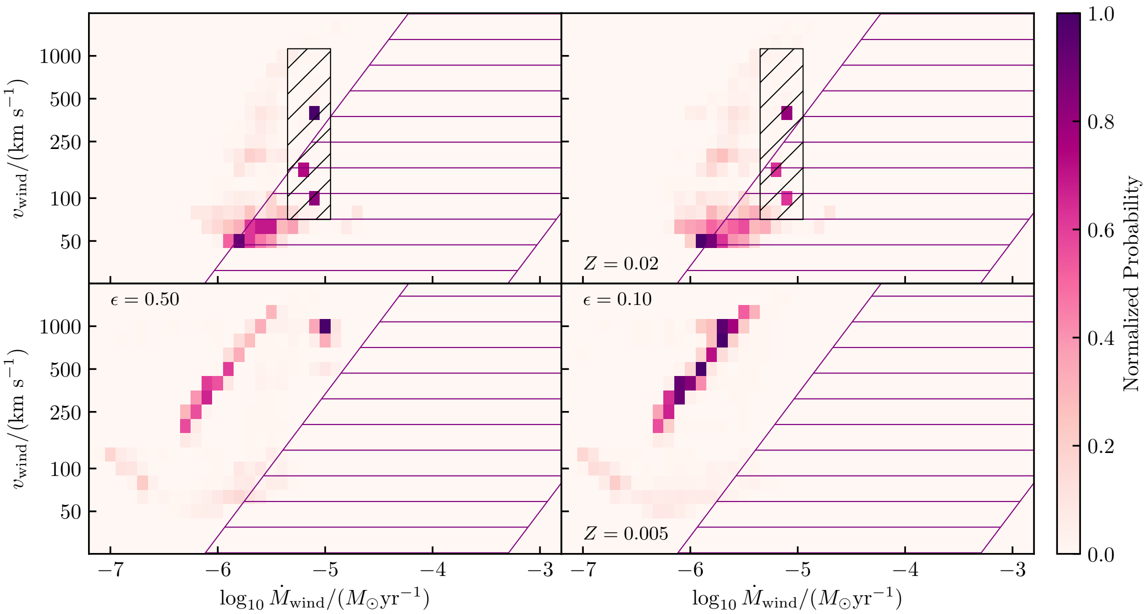

Figure 6.3 Distributions of CSM properties of single and binary ($\epsilon = 0.1$ (right) and 0.5 (left)) SNe IIb at solar (top) and low metallicity (bottom), shaped by the progenitor system at the fiducial evolutionary stopping condition (0.1-100 years before progenitor CC) used in our models. The black diagonally-hatched region shows analogous results for single SNe IIb with normalized posterior probabilities ≥ 0.01. Purple horizontally-hatched region shows the range inferred for SNe IIb (Krauss et al., 2012; Kamble et al., 2016) from X-ray/radio observations. CSM for binary SNe IIb are less dense at low metallicity due to smaller progenitor radii resulting in higher wind velocities (mass loss rates are similar at low and high metallicities). Binary SNe IIb with $\log_{10}(P_{\rm orb,ZAMS}/{\rm d}) \gtrsim 2.8$ and single stars at solar metallicity match observational constraints for CSM properties (though only on the lower end) for SNe IIb; also see Figure 6.4 for the distribution of properties of these systems only at low metallicity.

the existence of blue (MS) companions with $\sim 10^{2.7} - 10^{5.2}\ L_\odot$ and red and yellow (at high metallicity and MT efficiency) companions with $\sim 10^{4.4} - 10^{5.4}\ L_\odot$.

6.3. Properties of Circumstellar Mediums

Figure 6.3 shows the distributions of CSM properties of single and binary SNe IIb at solar and low metallicity, shaped by the progenitor system at the fiducial

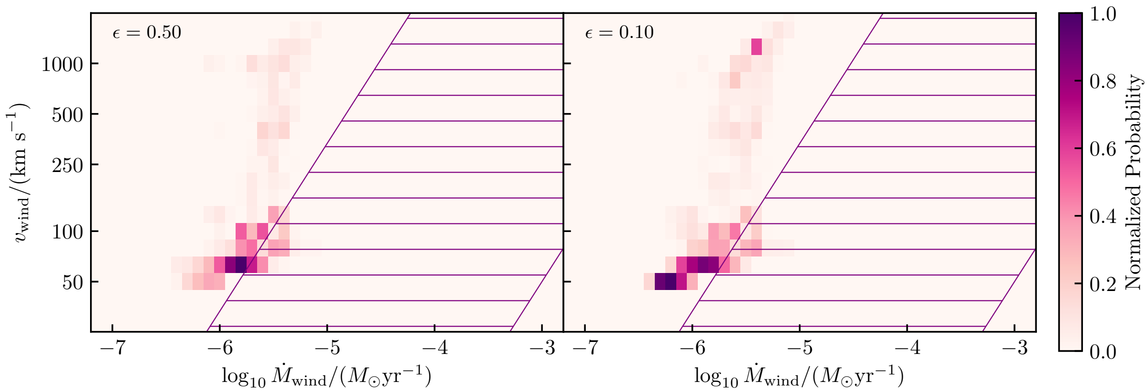

Figure 6.4 Similar to Figure 6.3 but only showing binary SNe IIb with $\log_{10}(P_{\rm orb,ZAMS}/{\rm d}) \gtrsim 2.8$ at low metallicity.

evolutionary stopping condition (0.1-100 years before progenitor CC) used in our models. Assuming that the SN shock is much faster than the CSM wind velocity, this corresponds to a range in CSM radii $\sim 10^{14} - 5 \times 10^{17}$ cm. To estimate the evolutionary state of our models at a certain number of years before CC (which is different from the fiducial evolutionary stopping condition used in our models), we run toy single star models with no stellar winds until the central silicon mass fraction drops below 10^{-6} and estimate (linear fits) the time to 'true' CC as a function of their helium/carbon core mass. We then use this relation to interpolate or extrapolate the progenitor properties in their past or future (since models have converged by the fiducial evolutionary stopping criterion to that at CC), respectively. We note that, our toy models with helium core masses $\lesssim 4 M_\odot$ ignite neon off-center and do not reach silicon core exhaustion. We ignore these models when computing the relation between helium core mass and time until CC. As a result, estimates of CSM properties for SNe IIb with helium core masses $\lesssim 4M_\odot$ should be interpreted with caution.

We assume that the wind velocity is equal to the escape velocity at the region being probed. Therefore, our computed wind velocities should be to be considered upper limits.

CSM for binary SNe IIb at low metallicities is less dense than at solar. This is because binary SNe IIb progenitors at low metallicities are more compact (see Section 6.1) and therefore have higher wind velocities; mass loss rates at both metallicities are similar. Observationally constrained CSM properties for SNe IIb are consistent with (though only on the low side) single SN IIb progenitors at low metallicity and binary SN IIb progenitors with $\log_{10}(P_{\rm orb,ZAMS}/{\rm d}) \gtrsim 2.8$ at both metallicities (see Figure 6.4 for a CSM properties at low metallicity for this group only). Note that since there is a bias towards detecting brighter events in X-rays/radio, the non-representation of CSM properties of SNe IIb progenitors with $\log_{10}(P_{\rm orb,ZAMS}/{\rm d}) \lesssim 2.8$ in observations cannot be used to rule this channel out. Alternately, it could also indicate eruptive mass loss in the progenitors (Quataert & Shiode, 2012; Shiode & Quataert, 2014; Strotjohann et al., 2015; Fuller, 2017).

CHAPTER 7

Relationships Between Progenitor Properties and Channels

Figure 7.1 shows the distribution of progenitor radius and effective temperature as a function of hydrogen envelope mass for binary SNe IIb at solar metallicity. This relation also exists at low metallicity but we don't show it here because the distribution is dominated by the group of compact progenitors (see Section 6.1) showing a large spread in effective temperature due to the helium main sequence (see below). Progenitors with smaller (larger) envelope masses are more compact (extended) and blue (red). This is because progenitors that experience progressively severe stripping begin resembling hydrogen-deficient Wolf-Rayet stars, which are hot and blue.

Figure 7.2 shows the distribution of progenitor helium core mass as a function of effective temperature for binary SNe IIb at solar and low metallicity. The distributions of the group of compact progenitors at low metallicity follows that on the H-R diagram. This is because SN IIb progenitor luminosities are determined by the helium core (which is formed during the MS). Since these progenitors only have a tenth of a solar mass of hydrogen envelope, their effective temperature distribution follows the helium ZAMS.

Finally, Figure 7.3 shows the distribution of initial orbital period as a function of progenitor hydrogen envelope mass for binary SNe IIb at solar and low metallicity. This figure shows that the group of compact progenitors are low metallicity arise from binaries that initiate MT on the HG. On the other hand, binary SNe IIb that initiate

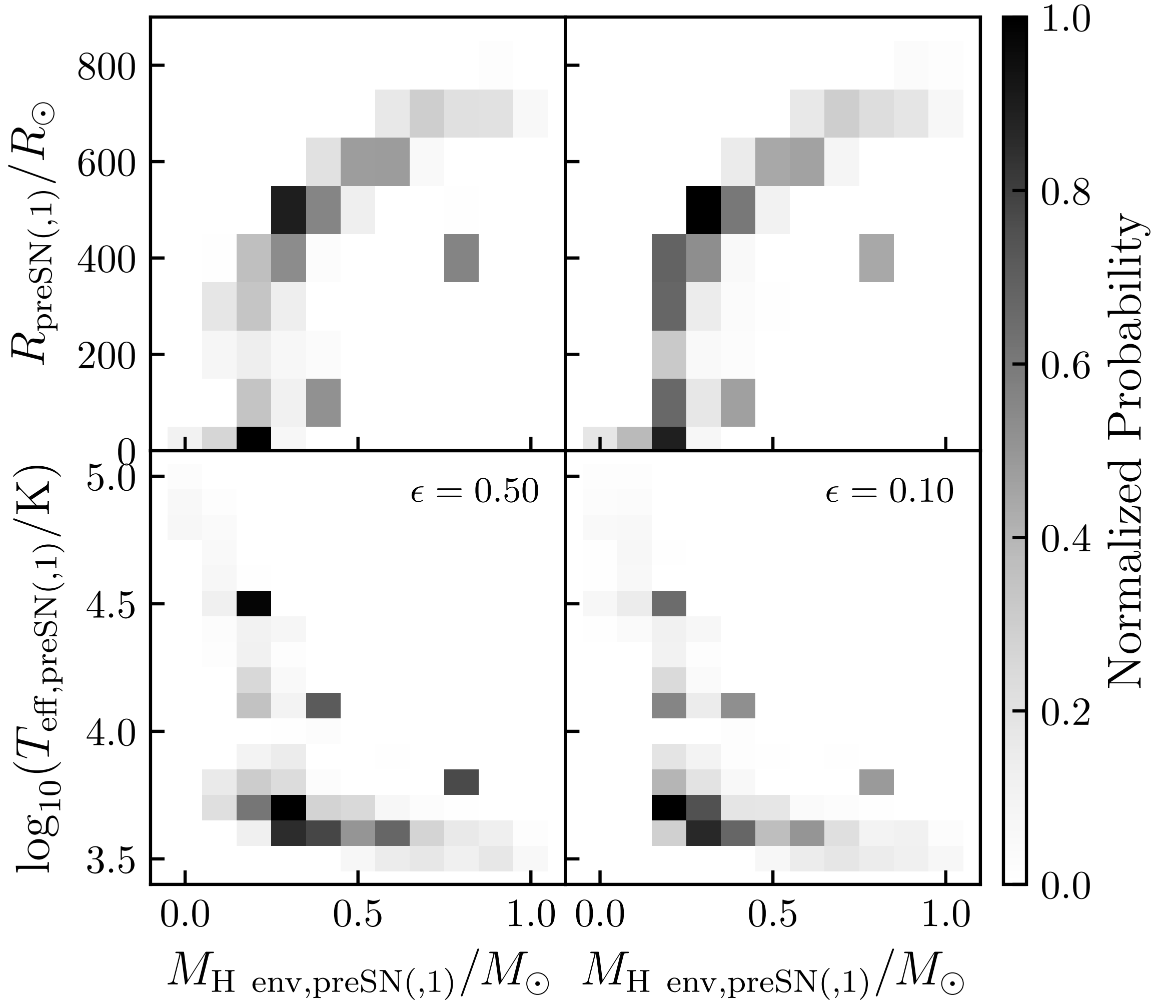

Figure 7.1 Distributions of progenitor radius ($R_{\mathrm{preSN}(,1)}$, top) and effective temperature ($T_{\mathrm{eff,preSN}(,1)}$, bottom) as a function of hydrogen envelope mass $M_{\mathrm{H\ env,preSN}(,1)}$, left) for binary SNe IIb with $\epsilon = 0.1$ (right) and 0.5 (left) at solar metallicity.

MT on the GB or later have a wide range in progenitor hydrogen envelope masses that also tend to be more massive.

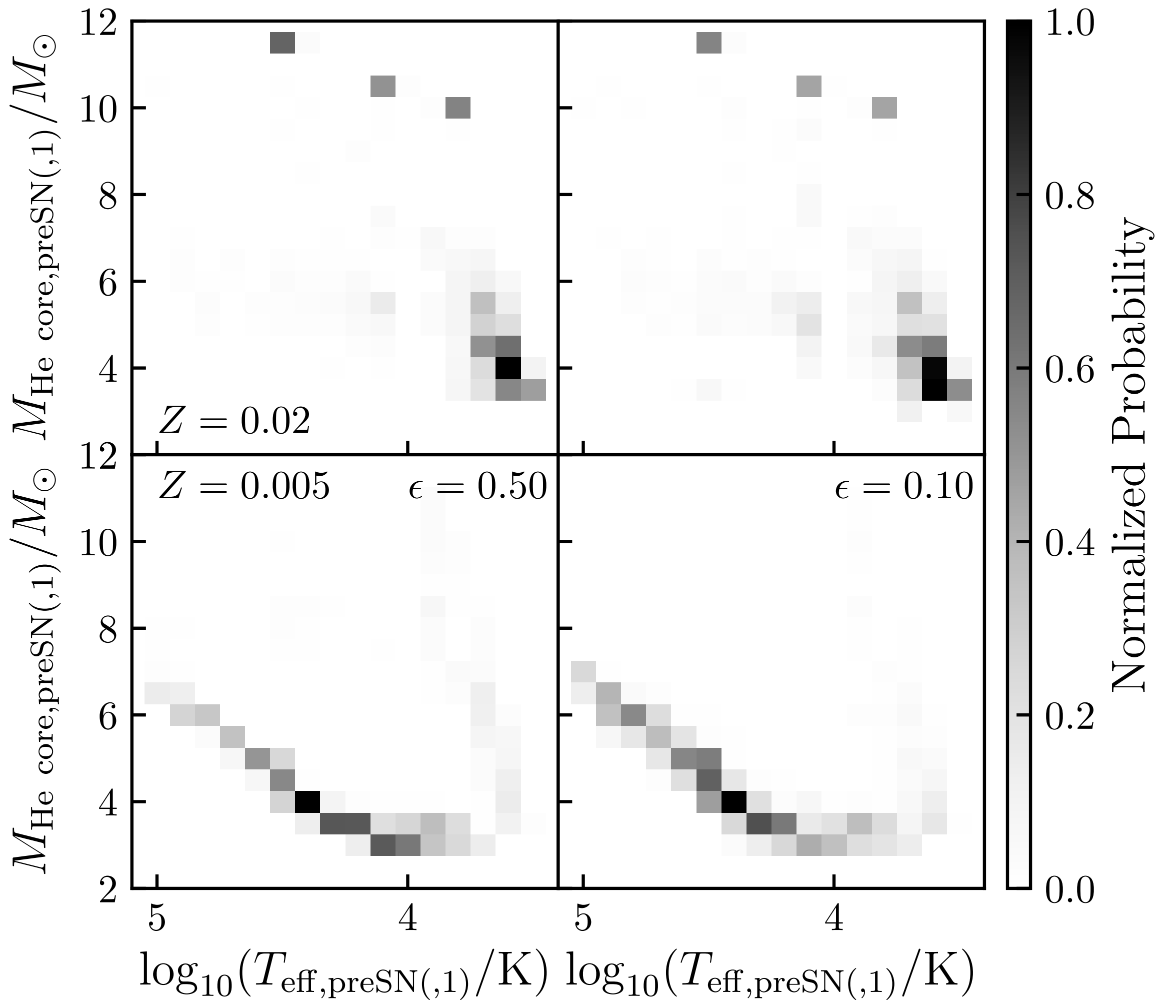

Figure 7.2 Distributions of progenitor helium core mass ($M_{\rm He\ core,preSN(,1)}$) as a function of effective temperature ($T_{\rm eff,preSN(,1)}$) for binary SNe IIb with $\epsilon = 0.1$ (right) and 0.5 (left) at solar (top) and low metallicity (bottom).

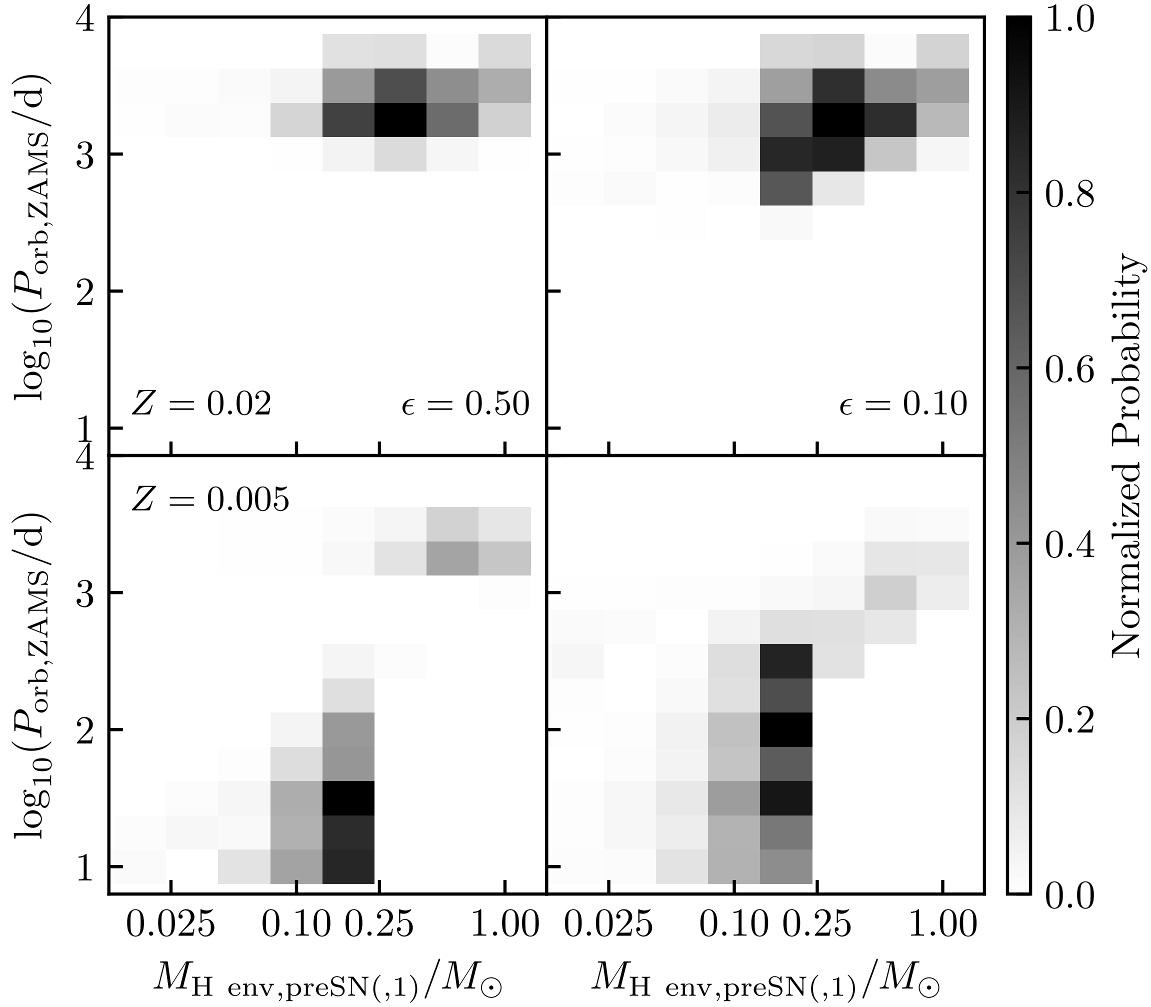

Figure 7.3 Distributions of initial orbital period ($P_{\rm orb,ZAMS}$) as a function of progenitor hydrogen envelope mass ($M_{\rm H\ env,preSN(,1)}$) for binary SNe IIb with $\epsilon = 0.1$ (right) and 0.5 (left) at solar (top) and low metallicity (bottom).

CHAPTER 8

Constraints on the Progenitor System of SN 2016gkg: A Case Study

8.1. Introduction

The mechanisms driving the stripping of the progenitor stars of stripped-envelope (SE) supernovae (SNe) remain an open research question. Currently, close binary interactions, stellar winds, and nuclear burning instabilities are leading candidates to explain the mass loss (e.g., Claeys et al., 2011; Arnett & Meakin, 2011; Groh et al., 2013b; Smith, 2014; Soker, 2017). Among SE SNe, Type IIb SNe explode with a low-mass residual hydrogen-envelope (e.g., Podsiadlowski et al., 1992; Woosley et al., 1994) and initially exhibit prominent hydrogen spectral features that weaken and disappear in the weeks following the explosion. The progenitors of five Type IIb SNe have been identified in pre-explosion images: 1993J (Aldering et al., 1994), 2008ax (Folatelli et al., 2015), 2011dh (Maund et al., 2011; Van Dyk et al., 2011), 2013df (Van Dyk et al., 2014), and 2016gkg (Kilpatrick et al., 2017). Furthermore, there is evidence for the presence of binary companions to the progenitors of SNe 1993J and 2011dh (Fox et al., 2014; Folatelli et al., 2014a). This makes Type IIb SNe ideal candidates to test theories of binary evolution.

SN 2016gkg was discovered on 2016 September 20.18 UT in NGC 613. Kilpatrick et al. (2017) identified a source in pre-explosion Hubble Space Telescope (HST) images

Table 8.1. Properties of Detected SN 2016gkg Progenitor

$\log_{10}(L/L_\odot)$	$T_{\rm eff}$/K	$R/R_\odot$	$M_{\rm env}/M_\odot$
$5.14^{+0.36}_{-0.14}$ [a]	9500^{+3700}_{-1033} [a]	$40 - 150$ [b]	$0.02 - 0.4$ [b]

References. — [a] Kilpatrick, C. D., private communication (uncertainties are one-third of 3σ, see Section 8.2.2); [b] Arcavi et al. (2017).

as its progenitor and inferred its luminosity and effective temperature. Tartaglia et al. (2017) found an additional source and concluded they could not favor either source as the progenitor star. They also found different magnitudes for the common source. The properties for this source inferred by Tartaglia et al. (2017) are consistent (within 1 and 3σ in luminosity and effective temperature, respectively) with those inferred by Kilpatrick et al. (2017). Therefore, for simplicity, we adopt the constraints of Kilpatrick et al. (2017). Arcavi et al. (2017) fit analytic models to the light curve of SN 2016gkg and derived a radius and residual hydrogen-envelope mass for the progenitor star (see Table 8.1).

In this paper, given observational constraints on its progenitor properties, we use Bayesian inference to derive the distribution of properties of potential progenitor systems (both singles and binaries) of SN 2016gkg. We also calculate the probability that the progenitor was a binary. We assume that the constraints derived by Kilpatrick et al. (2017) corresponds to the progenitor. We discuss the effect of using the pre-SN progenitor hydrogen-envelope and helium-core mass constraints to distinguish between single and binary progenitor channels.

This paper is organized as follows. In Section 8.2 we briefly describe our models and method. In Section 8.3 we discuss results for the distribution of potential progenitor systems (both singles and binaries) of SN 2016gkg. We summarize our results and conclude in Section 8.4.

8.2. Method

8.2.1. Single and Binary Star Models

We compute a large grid of non-rotating solar-metallicity[1] single and binary star models with Modules for Experiments in Stellar Astrophysics (`MESA`[2], Paxton et al., 2011, 2013, 2015). We briefly summarize the models in what follows.

We start the evolution of the star(s) at the zero-age main sequence (ZAMS). We stop the evolution if any of the following conditions are met: the carbon mass fraction at (any) star's center is lower than 10^{-6}, the hydrogen-envelope mass of any star drops below $0.01 M_\odot$ (in which case we assume the system is a completely stripped Type Ibc progenitor), or, in binaries, the accretor overfills its Roche-lobe. We assume the surface properties of the star at carbon depletion match those of the pre-supernova progenitor star. This is because the thermal timescale of the envelope is large compared to the time between carbon depletion and iron core-collapse. We note however that it has recently been proposed that waves could efficiently transport energy outwards during core neon and oxygen burning, potentially producing outbursts and large changes in the progenitor surface luminosity and effective temperature months

[1]We choose the value of solar metallicity ($Z_\odot$) to be 0.02. The metallicity of the host galaxy of SN 2016gkg is 0.012 ± 0.004 (Kilpatrick et al., 2017). See Conclusions for a discussion on the effect of metallicity.

[2]Release 9575.

or years prior to the explosion (Quataert & Shiode, 2012; Shiode & Quataert, 2014; Fuller, 2017).

We use the `basic.net`, `approx21.net`, and `co_burn .net` nuclear networks in `MESA`. We adopt the standard mixing-length theory and the Ledoux criterion to model convection, with $\alpha_{\rm MLT}$ set to 1.5. When convective regions approach the Eddington limit, the efficiency of convection is enhanced[3] (Paxton et al., 2013). To account for the nonzero momentum of a convective element at the Hydrogen burning convective core boundary, we extend this region by 0.335 of the pressure scale height (Brott et al., 2011). We adopt the value of dimensionless free parameter for semi-convection, $\alpha_{\rm sc}$, to be 1.0 (Yoon et al., 2006). We use radiative opacity tables from the OPAL project (Iglesias & Rogers, 1996). We adopt surface effective temperature and abundance dependent stellar wind prescriptions. When $T_{\rm eff} > 10^4\,{\rm K}$, we adopt the prescription of Vink et al. (2001) if the surface hydrogen mass fraction > 0.4 and Nugis & Lamers (2000) otherwise. If $T_{\rm eff} < 10^4\,{\rm K}$ we adopt the prescription of de Jager et al. (1988).

We use the model of Kolb & Ritter (1990) to calculate the mass transfer rate due to Roche-lobe overflow (RLO) in our binary star models. The efficiency of mass transfer (the ratio of mass accreted by the secondary to the mass transferred via RLO by the primary), ϵ, is assumed to be constant during the evolution. The mass not accreted is assumed to be lost as stellar winds. Stellar winds carry away with them the specific angular momentum of the corresponding component. All orbits are assumed to be circular.

[3]The treatment of these regions is a subject of debate and stellar evolution calculations during these phases are uncertain.

We compute single-star models with initial mass, $\log_{10}(M_{\rm ZAMS}/M_\odot) = 1.28 - 1.40$ ($M_{\rm ZAMS}/M_\odot \sim 19 - 25$) in intervals of 0.0005 dex and binary star models with initial primary mass, $\log_{10}(M_{\rm ZAMS,1}/M_\odot) = 1.0 - 1.4$ ($M_{\rm ZAMS,1}/M_\odot \sim 10 - 25$) in intervals of 0.02 dex, initial mass ratio, $q_{\rm ZAMS} \equiv M_{\rm ZAMS,2}/M_{\rm ZAMS,1} = 0.225 - 0.975$ in intervals of 0.05, and initial orbital period, $\log_{10}(P_{\rm orb}/{\rm d}) = 2.5 - 3.8$ ($P_{\rm orb}/{\rm d}\sim 316 - 6310$) in intervals of 0.02 dex[4]. We choose this parameter space based on a broader scan. We compute the models for $\epsilon = 0.5$ and 0.1. Models that reach core carbon exhaustion ($C_{\rm center} \leq 10^{-6}$) with less than $1M_\odot$ (but greater than $0.01M_\odot$) of residual hydrogen-envelope are defined as Type IIb SN progenitors. This criterion is a conservative choice as residual hydrogen envelope masses of Type IIb SNe with detected progenitors are less than $0.5M_\odot$ (Woosley et al., 1994). Type IIb SNe with detected progenitors represent those with the most massive envelopes: progenitors with smaller envelopes are compact (Yoon et al., 2017) and thus harder to detect. Moreover, the cooling envelope feature in Type IIb SN light curves decrease with decreasing radius (Moriya et al., 2016) and envelope mass making compact Type IIb SNe harder to detect.

8.2.2. Statistical Method

We use Bayesian inference to derive the distribution of the potential progenitors (and their binary companions) of SN 2016gkg. We adopt 3σ (see below for reasoning) luminosity and effective temperature constraints on the progenitor as derived from observations of the progenitor system before explosion (Kilpatrick, C. D., private

[4] `MESA` inlists used for these can be found at `https://github.com/orlox/mesa_input_data/tree/master/2017_IIb`

communication). We assume that luminosity and effective temperature are independent variables for simplicity, though this assumption is not accurate. We do not apply the progenitor hydrogen-envelope mass and radius constraints derived from the SN light-curves as these are model-dependent. However, we discuss the implications of applying them later.

For each Type IIb SN progenitor model (see above for definition) we compute a posterior probability (P):

$$P(\vec{\theta}_{\rm mod}|\vec{X}_{\rm obs}) = \mathcal{L}(\vec{X}_{\rm obs}|\vec{\theta}_{\rm mod})P(\vec{\theta}_{\rm mod}), \tag{8.1}$$

modulo the standard normalization constant in Bayes' theorem. The model parameters, $\vec{\theta}_{\rm mod}$, are the initial single (initial mass) or binary (initial primary mass, mass ratio, and orbital period) star progenitor properties and eventually determine the pre-SN progenitor properties, $\vec{X}_{\rm mod}$, i.e., $\vec{X}_{\rm mod}(\vec{\theta}_{\rm mod})$. For each individual observable quantity $X_{\rm obs,i}$ (the i-th component of vector $\vec{X}_{\rm obs}$) with mean, $\mu_{\rm i}$, and uncertainties, $\sigma_{+/-,\rm i}$, we adopt the split normal distribution for the likelihood

$$\begin{aligned}\mathcal{L}(\mu_{\rm i}, \sigma_{+,\rm i}, \sigma_{-,\rm i}|X_{\rm mod,i}) =& \sqrt{\frac{2}{\pi}}\frac{1}{\sigma_{-,\rm i} + \sigma_{+,\rm i}} \times \\ & \exp\left(-\frac{(X_{\rm mod,i} - \mu_{\rm i})^2}{2\sigma_{\rm i}^2}\right)\end{aligned} \tag{8.2}$$

where $\sigma_{\rm i} = \sigma_{-,\rm i}$ when $X_{\rm mod,i} < \mu_{\rm i}$ and $\sigma = \sigma_{+,\rm i}$ when $X_{\rm mod,i} \geq \mu_{\rm i}$. For each individual observable quantity $X_{\rm obs,i}$ with a range of values, we adopt a flat distribution for the likelihood. Thus,

$$\mathcal{L}(\vec{X}_{\rm obs}|\vec{\theta}_{\rm mod}) = \prod_{\rm i} \mathcal{L}(\mu_{\rm i}, \sigma_{+,\rm i}, \sigma_{-,\rm i}|X_{\rm mod,i}) \tag{8.3}$$

Observational uncertainties are not necessarily distributed as a normal distribution and this form of the likelihood function is just an approximation. In particular, the 1σ range for luminosity and effective temperature from Kilpatrick et al. (2017) is much wider than one-third of their 3σ range (Kilpatrick, C. D., private communication). To avoid artificially extending the range of uncertainty in the observations, we adopt σ_+ and σ_- to be one-third of the respective $3\sigma_+$ and $3\sigma_-$ values instead of the $1\sigma_{+/-}$ values in Kilpatrick et al. (2017).

The prior probability $P(\vec{\theta}_{\rm mod})$ is computed for the range $[\vec{\theta}_{\rm mod} - \Delta\vec{\theta}_{\rm mod}/2, \vec{\theta}_{\rm mod} + \Delta\vec{\theta}_{\rm mod}/2]$. For a single-star with initial mass, $\log_{10} M_{\rm ZAMS}$,

$$P(\vec{\theta}_{\rm mod}) = (1 - f_{\rm bin})P(\log_{10} M_{\rm ZAMS}) \tag{8.4}$$

and for a stellar binary with initial primary mass, $\log_{10} M_{\rm ZAMS,1}$, initial mass ratio, $q_{\rm ZAMS}$, and initial orbital period, $P_{\rm orb}$,

$$P(\vec{\theta}_{\rm mod}) = f_{\rm bin}P(\log_{10} M_{\rm ZAMS,1})P(q_{\rm ZAMS}) \\ P(\log_{10} P_{\rm orb}) \tag{8.5}$$

where, $f_{\rm bin}$ is the fraction of stars in binaries.

We assume $f_{\rm bin}$ to be a constant and independent of M, q, and $P_{\rm orb}$. The distribution of M is taken to be the Salpeter Initial Mass Function (IMF, Salpeter, 1955)

$$f(M) = M^{-\alpha}; \tag{8.6}$$

We assume that the minimum ZAMS mass needed to undergo core-collapse is $8M_{\odot}$ (Woosley et al., 2002). We adopt a power-law distribution for the initial mass ratio, q,

$$f(q) = q^{\beta} \tag{8.7}$$

This distribution is assumed to be followed for $q > 0.2$ (Kobulnicky et al., 2014). Finally, the distribution of initial orbital period, $P_{\rm orb}$, is chosen according to Kobulnicky et al. (2014)

$$f(\log_{10} P_{\rm orb}) = (\log_{10} P_{\rm orb})^{\gamma} \tag{8.8}$$

This distribution is assumed to hold[5] for $0.15 < \log_{10}(P_{\rm orb}/{\rm d}) < 4$.

8.3. Results

We compute posterior probabilities for SN 2016gkg using our model Type IIb SN progenitors (see Section 8.2.1 for definition) using the method described above. Unless otherwise mentioned, we assume $f_{\rm bin} = 0.5$, $\alpha = 2.3$ (Salpeter, 1955), β = -1, and $\gamma = -0.22$ (Kobulnicky et al., 2014).

[5]The upper limit for the validity of this distribution is 2000 days (Kobulnicky et al., 2014). However, due to poor constraints for wide binaries we assume that this distribution holds up to 10,000 days.

Some binary star models experience very little interaction, transferring only small amounts of mass when the primary star's atmosphere Roche-lobe overflows. Therefore their evolution largely resembles that of single stars. We therefore require that primaries transfer at least 1% of their initial mass in RLO to qualify as 'binary' progenitors. The exact choice for this number does not affect our results significantly; lowering it by an order of magnitude adds some $\gtrsim 22M_{\odot}$ mass binaries with net posterior probabilities $\lesssim$3% more for our fiducial priors.

In figure 8.1 we show the distribution of the parameter space of potential single and binary star progenitors of SN 2016gkg. There are three peaks in the distribution of initial primary mass for binary star progenitors. The low mass peak is favored by the prior on initial primary mass (Eq. 8.6), the middle peak is due to the likelihood for $T_{\rm eff}$, and the high mass peak results from mildly interacting binaries with relatively undisturbed primaries whose evolution largely resembles their single-star counterparts. There are fewer binary star progenitors with $\epsilon = 0.5$, $q_{\rm ZAMS} > 0.7$, and $\log_{10}(P_{\rm orb}/{\rm d}) \lesssim 3.1$ as they experience unstable mass transfer or evolve into contact, which lead to a merger.

In figure 8.2 we show the distribution of pre-SN properties of potential single and binary star progenitors of SN 2016gkg. The three peaks in the distributions of initial primary mass (Figure 8.1) of binary star progenitors roughly translate to the distributions of pre-SN hydrogen-envelope and helium-core mass. Pre-SN hydrogen-envelope and helium-core mass for potential binary star progenitors are clearly smaller than for potential single-star progenitors (e.g., Podsiadlowski et al., 1992; Yoon et al., 2010; Claeys et al., 2011) typically by $0.1M_{\odot}$ and $2M_{\odot}$, respectively. Therefore, these can be used to distinguish progenitor scenarios. While progenitor helium-core mass constraints are currently unavailable for SN 2016gkg, their existence could increase the likelihood of a binary progenitor of SN 2016gkg significantly by ruling out several single-star progenitors (see below for a discussion on rates). The distribution of all binary star properties shown in Figures 8.1 and 8.2 remain roughly the same regardless of whether or not we apply model-dependent progenitor hydrogen-envelope mass and radius constraints.

In figure 8.3 we show the distribution of locations on the Hertzsprung-Russell (H-R) diagram of potential single and binary star progenitors of SN 2016gkg. The luminosities of binary progenitors are smaller than of single-star progenitors. This is a consequence of smaller pre-SN helium-core masses for binary progenitors (see Figure 8.2). The secondaries of binary progenitors mostly lie on the main-sequence and are less luminous than their primaries with $M_{\rm bol} \gtrsim -8.5$. Some binary progenitors with initial mass ratios ~ 1 have evolved secondaries that are on the red-giant branch (RGB). We find that it is unlikely for the secondary to lie between the main sequence and the RGB, which is the case for the companion of SN 1993J (Maund et al., 2004). Otherwise, no strong constraints can be placed on binary companions' location on the H-R diagram. We also note that in binaries with secondaries of luminosities similar to that of the primary, flux from the secondary may contaminate flux from the primary, making our calculations inconsistent with the derivation of observed constraints. We find that the total posterior probability of progenitors having secondaries with luminosities within a factor of 2 of the primary (and thus potentially contaminated) is $\sim 12\%$ for $\epsilon = 0.1$ and $\sim 4\%$ for $\epsilon = 0.5$.

Table 8.2. Probability of a binary star progenitor of SN 2016gkg

α	β	γ	$P_{\rm binary} \mid L, T_{\rm eff}$		$P_{\rm binary} \mid L, T_{\rm eff}, M_{\rm env}, R$	
			$\epsilon = 0.1$	$\epsilon = 0.5$	$\epsilon = 0.1$	$\epsilon = 0.5$
1.6	-2.0	0.00	0.13	0.08	0.28	0.17
		-0.22	0.11	0.06	0.25	0.15
	-1.0	0.00	0.21	0.12	0.42	0.26
		-0.22	0.18	0.11	0.38	0.23
	0.0	0.00	0.29	0.17	0.52	0.34
		-0.22	0.25	0.15	0.48	0.30
2.3	-2.0	0.00	0.16	0.10	0.34	0.22
		-0.22	0.14	0.08	0.31	0.19
	-1.0	0.00	0.25	0.15	0.48	0.32

X-ray/radio observations can be used to infer the CSM density around SN progenitors and thus trace the mass loss history of the progenitor star. We use our models to infer the CSM density at 10^{16} cm to compare with the results of Margutti et al. (2017) (example Figure 6). Our models have a SN Ibc-like mass loss history: $v_{\rm wind} \sim 50 - 250$ km s^{-1} and $\dot{M}_{\rm wind} \sim 10^{-4.8} - 10^{-6} M_\odot$ yr^{-1}. This is because all potential binary progenitors detach before core-collapse. If future measurements indicate that SN 2016gkg also experienced high mass-loss rates ($\sim 10^{-4} M_\odot$ yr^{-1}), like those for other Type IIb SNe in the aforementioned study, then it would indicate that the progenitor experienced a period of enhanced mass loss just before explosion.

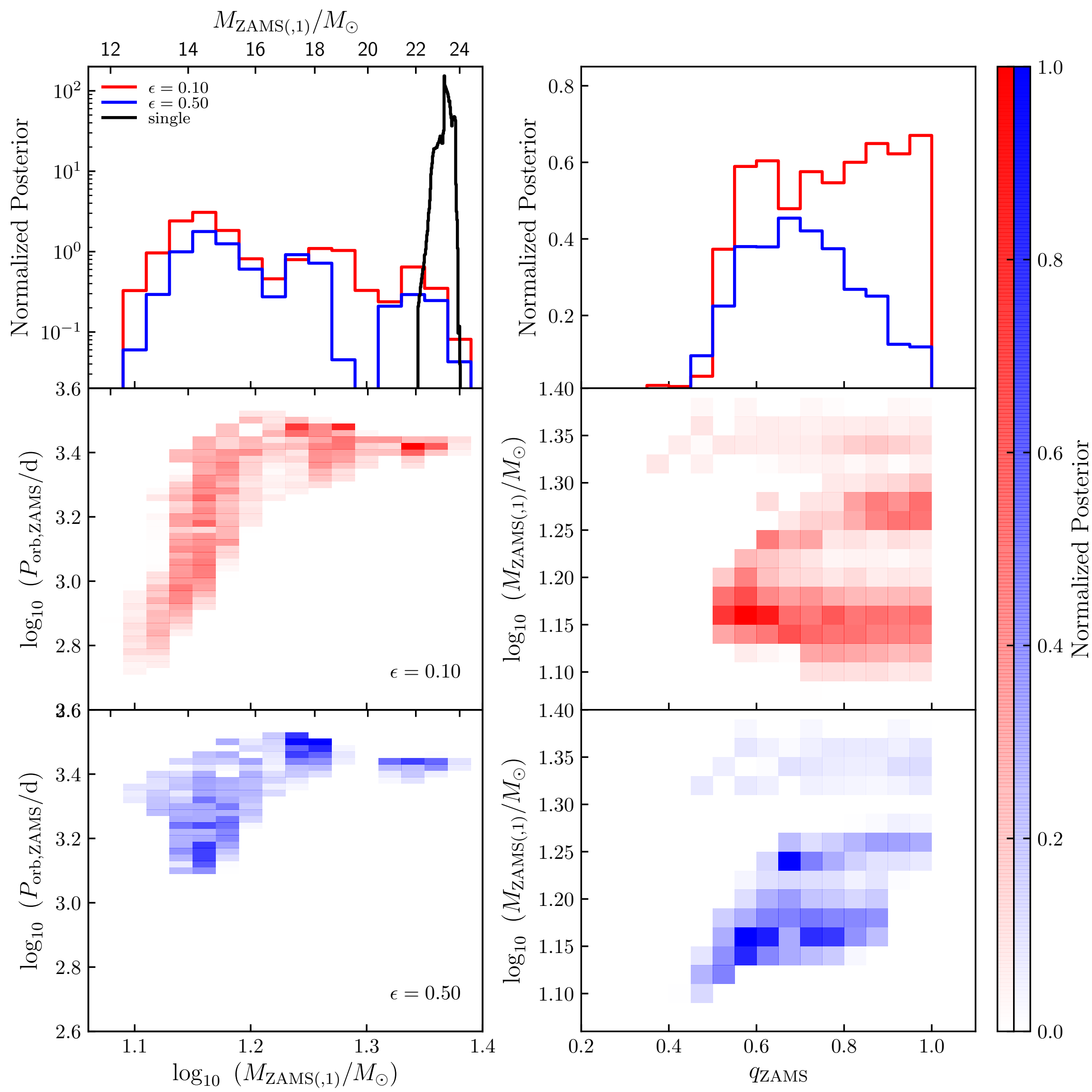

Figure 8.1 Posterior probability distributions of the parameter space of potential single and binary star progenitors of SN 2016gkg. The top panel shows the distribution of initial (primary) mass ($M_{ZAMS(,1)}$, left) and, for binaries, initial mass ratio ($q_{ZAMS} \equiv M_{ZAMS,2}/M_{ZAMS,1}$, right) of potential single (black) and binary star progenitors with $\epsilon = 0.1$ (red) and 0.5 (blue). The histograms show the total posterior probability in each bin. The histograms in the top left panel have been rescaled such that areas under them reflect the probability of a single or binary star progenitor of SN 2016gkg. The middle and bottoms panels show 2-D distributions of P_{orb} and $M_{ZAMS(,1)}$ (left) and $M_{ZAMS(,1)}$ and q_{ZAMS} (right) of potential binary star progenitors with $\epsilon = 0.1$ (middle) and 0.5 (bottom).

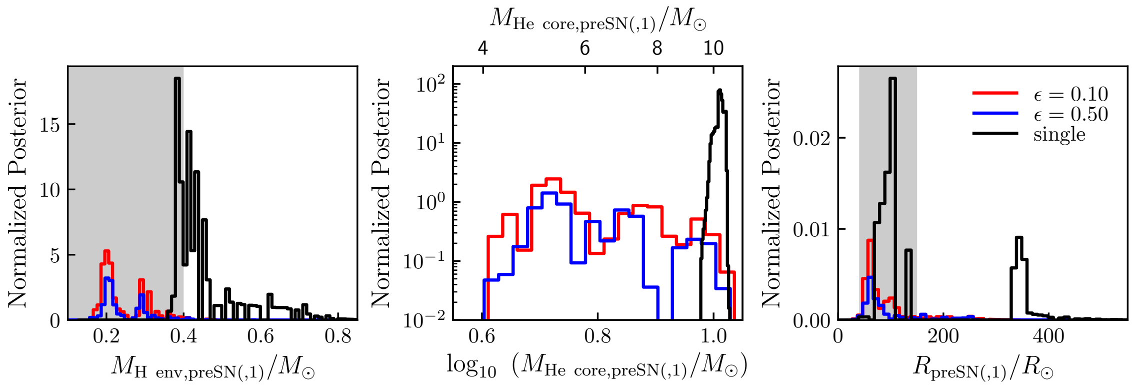

Figure 8.2 Distributions of pre-SN properties of potential single (black) and binary ($\epsilon = 0.1$ (red) and 0.5 (blue)) star progenitors of SN 2016gkg: progenitor hydrogen-envelope mass ($M_{\rm H\ env,preSN(,1)}$, left), progenitor helium-core mass ($M_{\rm He\ core,preSN(,1)}$, middle), and progenitor radius ($R_{\rm preSN(,1)}$, right). The histograms show the total posterior probability in each bin and have been rescaled such that areas under them reflect the probability of a single or binary star progenitor of SN 2016gkg. Grey shaded regions indicate constraints derived from light-curves (see Table 8.1). Pre-SN hydrogen-envelope and helium-core mass for potential binary star progenitors are smaller than for potential single-star progenitors typically by $0.1M_\odot$ and $2M_\odot$, respectively. Constraints on the progenitor hydrogen-envelope mass and radius from light-curves increase the likelihood of a binary progenitor of SN 2016gkg from 22% (13%) to 44% (28%) for $\epsilon = 0.1$ (0.5).

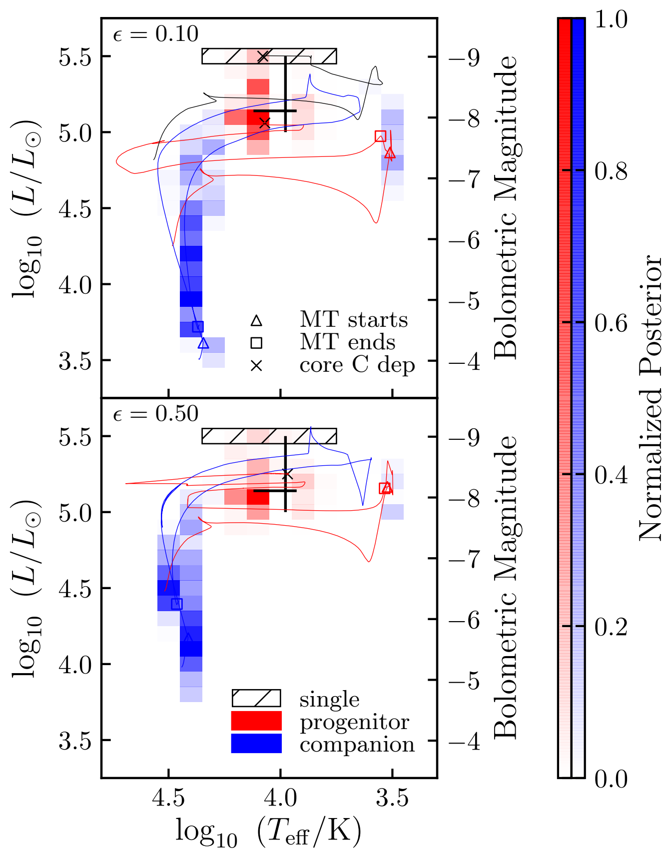

Figure 8.3 Distributions of H-R locations of potential single and binary ($\epsilon = 0.1$ (top) and 0.5 (bottom)) star progenitors of SN 2016gkg. The red (blue) color scales show distributions for the primary (secondary) of binary star progenitors. Red (blue) H-R tracks are for the primary (secondary) of the binary star model with the highest posterior probability for the corresponding ϵ: $M_{\rm ZAMS,1} = 14.45$ (17.38) $M_\odot$, $q_{\rm ZAMS} \equiv M_{\rm ZAMS,2}/M_{\rm ZAMS,1} = 0.575$ (0.675), and $P_{\rm orb} = 2291$ (3311) days for $\epsilon = 0.1$ (0.5). Mass transfer (MT) is defined to be taking place when mass transfer rate due to RLO is $\geq 10^{-6} M_\odot$ yr^{-1}. The black H-R track is for the single-star model with the highest posterior probability: $M_{\rm ZAMS} = 23.28$ $M_\odot$. The hatched region shows H-R locations of potential single-star progenitors with normalized posterior probabilities ≥ 0.01. Black error-hairs show one-third of the 3σ constraints on the observed progenitor for SN 2016gkg (Table 8.1). If present, the binary companion of SN 2016gkg has $M_{\rm bol} \gtrsim -8.5$ and is a main-sequence or red-giant star (for binary star progenitors with initial mass ratios ~ 1). As such no strong constraints can be placed on the companion.

Table 8.2 (cont'd)

α	β	γ	$P_{\mathrm{binary}}\|L, T_{\mathrm{eff}}$		$P_{\mathrm{binary}}\|L, T_{\mathrm{eff}}, M_{\mathrm{env}}, R$	
			$\epsilon = 0.1$	$\epsilon = 0.5$	$\epsilon = 0.1$	$\epsilon = 0.5$
		-0.22	0.22	0.13	0.44	0.28
	0.0	0.00	0.34	0.21	0.59	0.40
		-0.22	0.31	0.18	0.55	0.36
3.0	-2.0	0.00	0.20	0.12	0.41	0.27
		-0.22	0.17	0.11	0.37	0.24
	-1.0	0.00	0.31	0.19	0.56	0.38
		-0.22	0.28	0.17	0.52	0.35
	0.0	0.00	0.41	0.25	0.66	0.47
		-0.22	0.37	0.22	0.62	0.43

Note. — $f_{\mathrm{bin}} = 0.5$, and α, β, and γ are parameters for the priors on the initial mass, $\log_{10} M_{\mathrm{ZAMS}}$, initial mass ratio, q_{ZAMS}, and initial orbital period, P_{orb}, respectively (see Eqs. 8.6, 8.7, and 8.8).

Finally, we compute the probability that the progenitor of SN 2016gkg was a binary: the total posterior probability of all model binary star progenitors divided by total posterior probability of all model single and binary star progenitors. In Table 8.2 we list probabilities of a binary star progenitor of SN 2016gkg not applying and applying model-dependent progenitor hydrogen-envelope mass and radius constraints, for $f_{\mathrm{bin}} = 0.50$ and various values of α, β, and γ. We find that the probability of a binary star progenitor of SN 2016gkg with $\epsilon = 0.1$ and 0.5 not-given (given) progenitor hydrogen-envelope mass and radius constraints is 22% (44%) and 13% (28%, respectively, for our fiducial values of α (2.3), β (-1.0), and γ (-0.22).

8.4. Conclusions

We use Bayesian inference and a large grid of single and binary star models to derive the distributions of potential progenitors and companions of SN 2016gkg. We find that potential binary star progenitors have lower initial primary mass and pre-SN hydrogen-envelope and helium-core mass than single-star progenitors. The probability that the progenitor of SN 2016gkg was a binary with $\epsilon = 0.1$ (0.5) is 22% (13%) if we only use luminosity and effective temperature constraints on the progenitor star. Applying model-dependent observational constraints on the progenitor hydrogen-envelope mass and radius rule out several single-star progenitors, favoring a binary as the progenitor of SN 2016gkg (44% for $\epsilon = 0.1$ and 28% for $\epsilon = 0.5$). In either case, there is no clear preference for a binary star progenitor of SN 2016gkg. This is in contrast to binaries being the currently favored progenitors of Type IIb SNe. We find that, a binary companion, if present, has $M_{\rm bol} \gtrsim -8.5$ and is a main-sequence or red-giant star. As such, we are unable to find strong constraints on the nature of the companion star. Constraints on the progenitor helium-core mass can help tighten constraints on the progenitor. Similarly, improved constraints on the progenitor luminosity can significantly narrow the parameter space for progenitors. We would like to stress that the parameter space for Type IIb SN progenitors is strongly dependent on the progenitor metallicity. At lower metallicities, the parameter space for binary progenitors of Type IIb SNe widens significantly (Yoon et al., 2017). We expect that the results presented here will differ strongly at low metallicities with the probability of a binary progenitor increasing significantly. Nevertheless, the probability of a binary progenitor derived at solar metallicity represents a lower limit. At lower metallicities, the binary star channel towards Type IIb SNe dominates for a couple of reasons. First, the parameter space for binary star Type IIb SN progenitors widens significantly at lower metallicity (Yoon et al., 2017). Second, single star Type IIb SN progenitors are produced at higher masses (due to the scaling in wind mass-loss) and are thus disfavored by the IMF. A detailed investigation into the effects of metallicity on the relative importance of single and binary progenitors of Type IIb SNe would be an interesting line of future investigation.

CHAPTER 9

Future Work

9.1. Motivation

The physics of massive star evolution, especially those in late-stages, is quite uncertain. At the same time, the lives and deaths of massive stars are instrumental in shaping our Universe by injecting matter and energy into their vicinity, influencing the evolution of galaxies, future generations of stars and planets, and, as a result, life itself. Massive stars are also progenitors to some of the most exotic objects and phenomena in our Universe: neutron stars, black holes, and supernovae (SNe) to name very few. Thus, it is of paramount importance to understand the physics governing massive star evolution. Using observations to constrain theoretical models is the only way forward for real progress.

Two dominant uncertainties surrounding massive star evolution relate to wind mass loss and binary interaction. The progenitors of SNe that lose their outer layers before exploding (known as stripped-envelope [SE] SNe) are ideal candidates for investigating the two mechanisms as both are thought to play crucial roles in the evolution of their progenitor stars (e.g., Podsiadlowski et al. 1992; Yoon et al. 2010). Current methods of understanding SE SN progenitor channels do not take into account statistical properties of stellar populations and therefore fail to identify dominant channels. Such analyses however, are imperative given the rise of telescope surveys aimed at collecting as much data as possible in order to maximize the science gain from the data collected. In addition SE SNe are quite abundant, making up $\sim$ 30-37% of all core-collapse SNe (Smith et al. 2011, Shivvers et al. 2017), making them strongly conducive to statistical investigations.

For my post-doctoral research, I propose to use a large database of SE SN progenitors modeled self-consistently from birth to the explosion event to:

(1) derive statistically robust constraints on progenitor properties and relevant physics, given observations and

(2) propose observing strategies for transient telescope surveys to improve such constraints.

9.2. Methodology

A comprehensive database of complete evolutionary histories of SE SNe progenitors covering a broad parameter space is necessary, if one is to match pre-/post-explosion observed constraints to progenitor physics dominating much before the SN event. Unfortunately, such a database that properly accounts for theoretical physics uncertainities does not exist. The first phase of my project is to build this database. This will be done in two steps. First, I will model the full parameter space[1] of SE SN progenitors from birth to core-collapse using the full stellar structure and evolution code, MESA (Modules for Experiments in Stellar Astrophysics). For my thesis I have already computed a subset of this parent database by modeling SE SNe of Type

[1]in initial primary mass, mass ratio, orbital period, efficiency of mass transfer and metallicity

IIb from birth to core-collapse[2]. I will also recompute the models for different mass loss prescriptions as it is a dominant uncertainty in massive star evolution that can be constrained using SE SNe. I will also test sensitivity to other uncertain physics, in particular convection. In the second step, I will explode the pre-SN models to compute their light-curves. As in the earlier step, each model will be recomputed by varying dominant yet uncertain explosion physics like the Nickel mass and explosion energy. Once complete, the database will be used to compute predicted rates for SE SN and their sub-types along with distributions of their progenitor properties as a test of the models.

Given the full database, I will use all available observations for SE SNe (progenitor data and light-curves) to set 'priors' on the models. The 'priors' represent our confidence that the models are progenitors of SE SNe given our knowledge about known events. As will be discussed next, these 'priors' allow the option of taking observed constraints on known SE SNe (light curves, explosion energy, nickel mass, progenitor radius, helium core mass, and magnitudes (if detected in pre-SN images), etc.) into account when drawing inferences on a new event. The mathematical framework for the computation of 'priors' is similar to the one I used in my recent paper on SN 2016gkg (Sravan et al. 2018). *The resulting database will capture the full range of physics we want to understand and all our prior knowledge from observations.*

Next, I will use the database to address **two** problems. **First**, *given observations for a SE SN, progenitor data and light-curves, derive constraints on its progenitor*

[2]Type IIb SNe are the least severely stripped of SE SNe exploding with a low-mass residual hydrogen-rich envelope (e.g. Podsiadlowski et al. 1992, Woosley et al. 1994), initially exhibiting prominent hydrogen spectral features that weaken and disappear in the weeks following the explosion.

properties and physics. The method for this is similar to the one I used on my recent paper on SN 2016gkg albeit without light-curve information. The new tool will accommodate all information on the SN event in addition to information on all previously known SE SNe. Such a tool will be extremely useful, especially given the advent of LSST, not only to aid in expediting event characterization but also for strategizing follow-up, for example to search for binary companions to progenitors.

The **second** problem is *guiding observing strategies in the era of LSST to improve constraints on SE SN progenitors.* The current cadence planned for the LSST is expected to be too coarse for many types of science shifting the burden of following up alerts to smaller telescopes. Given the expected demand for follow-up, requests that maximize the science gain while minimizing resources will be extremely valuable. To this end, *I will develop the following machine-learning tool to propose targeted follow-up strategies.* First, using a framework similar to the one above, I will use the weighted parent database (using prior knowledge of SE SNe) to predict the probability that a given evolving light curve belongs to a SE SN. If the probability is greater than a certain threshold, a gaussian process model will predict 'future' light-curves in various bands. Bands and periods which won't be observed, given (known) observing schedules of all transient machines, and for which 'future' light curves have large uncertainties will be flagged as priority for follow-up. This method reduces the burden of follow-up by soliciting only crucial measurements while maximizing improvements on constraining the progenitor. I am confident in implementing this tool because of my training in machine-learning through a special graduate-level training program in data-science at Northwestern (IDEAS, ideas.ciera.northwestern.edu).

9.3. Scientific Impact

My proposal leverages the statistical power of large datasets to answer fundamental questions about massive star evolution. It is also novel in its usage of a large database of self-consistently modeled SN progenitors to map pre-/post- explosion observational constraints to physics dominating earlier in the progenitor's evolution. In addition, the tools I will develop will aid rapid characterization of events and propose strategies to help reduce load for followup in the era of LSST. These tools are also flexible in that the framework can easily be extended to other SN or event types if they can be modeled reliably.

9.4. Conclusions

In order to complete our understanding of our Universe, we need to understand the physics of how massive stars lead and end their lives. The era of time-domain big-data astronomy provides us an opportunity to investigate the mechanisms driving massive star evolution using new methods, in particular those of statistical inference and machine-learning. Our work demonstrates the importance of using statistical inference on a complete self-consistently computed database of models to properly constrain SN progenitors and progenitor channels. We also find that uncertainties in mass-loss have a strong affect on our conclusions. This motivates the possibility that statistical information on SE SN can, in turn, be used to constrain mass-loss and other uncertain physics. Such analyses are not just possible but also imperative with recent major advances time-domain astronomy. The tools I describe here will help us address important questions about the lives and deaths of massive stars using these methods. In addition, my expertise in modeling SE SN progenitors and training in data-science make me uniquely suited to accomplishing this project.

References

Aldering, G., Humphreys, R. M., & Richmond, M. 1994, AJ, 107, 662

Almeida, L. A., Sana, H., Taylor, W., et al. 2017, A&A, 598, A84

Arcavi, I., Gal-Yam, A., Kasliwal, M. M., et al. 2010, ApJ, 721, 777

Arcavi, I., Hosseinzadeh, G., Brown, P. J., et al. 2017, ApJL, 837, L2

Arnett, W. D., & Meakin, C. 2011, ApJ, 741, 33

Asplund, M., Grevesse, N., Sauval, A. J., & Scott, P. 2009, ARA&A, 47, 481

Bellm, E. 2014, in The Third Hot-wiring the Transient Universe Workshop, ed. P. R. Wozniak, M. J. Graham, A. A. Mahabal, & R. Seaman, 27–33

Bellm, E., & Kulkarni, S. 2017, Nature Astronomy, 1, 0071

Benvenuto, O. G., Bersten, M. C., & Nomoto, K. 2013, ApJ, 762, 74

Bersten, M. C., Benvenuto, O. G., Nomoto, K., et al. 2012, ApJ, 757, 31

Bersten, M. C., Folatelli, G., García, F., et al. 2018, *Nature*, 554, 497

Böhm-Vitense, E. 1958, ZAp, 46, 108

Braun, H., & Langer, N. 1995, A&A, 297, 483

Brott, I., de Mink, S. E., Cantiello, M., et al. 2011, A&A, 530, A115

Cao, Y., Kasliwal, M. M., Arcavi, I., et al. 2013, ApJL, 775, L7

Chevalier, R. A., & Soderberg, A. M. 2010, ApJL, 711, L40

Chiosi, C., Nasi, E., & Sreenivasan, S. R. 1978, A&A, 63, 103

Claeys, J. S. W., de Mink, S. E., Pols, O. R., Eldridge, J. J., & Baes, M. 2011, A&A,

528, A131

Cox, J. P., & Giuli, R. T. 1968, Principles of stellar structure

Crockett, R. M., Eldridge, J. J., Smartt, S. J., et al. 2008, MNRAS, 391, L5

de Jager, C., Nieuwenhuijzen, H., & van der Hucht, K. A. 1988, A&AS, 72, 259

Dessart, L., Hillier, D. J., Livne, E., et al. 2011, MNRAS, 414, 2985

Drout, M. R., Milisavljevic, D., Parrent, J., et al. 2016, ApJ, 821, 57

Ergon, M., Sollerman, J., Fraser, M., et al. 2014, A&A, 562, A17

Ergon, M., Jerkstrand, A., Sollerman, J., et al. 2015, A&A, 580, A142

Filippenko, A. V. 1988, AJ, 96, 1941

Filippenko, A. V., Li, W. D., Treffers, R. R., & Modjaz, M. 2001, in Astronomical Society of the Pacific Conference Series, Vol. 246, IAU Colloq. 183: Small Telescope Astronomy on Global Scales, ed. B. Paczynski, W.-P. Chen, & C. Lemme, 121

Filippenko, A. V., Matheson, T., & Ho, L. C. 1993, ApJL, 415, L103

Folatelli, G., Bersten, M. C., Kuncarayakti, H., et al. 2015, ApJ, 811, 147

Folatelli, G., Bersten, M. C., Benvenuto, O. G., et al. 2014a, ApJL, 793, L22

Folatelli, G., Bersten, M. C., Kuncarayakti, H., et al. 2014b, ApJ, 792, 7

Folatelli, G., Van Dyk, S. D., Kuncarayakti, H., et al. 2016, ApJL, 825, L22

Fox, O. D., Azalee Bostroem, K., Van Dyk, S. D., et al. 2014, ApJ, 790, 17

Fryer, C. L. 1999, ApJ, 522, 413

Fuller, J. 2017, MNRAS, 470, 1642

Georgy, C., Ekström, S., Meynet, G., et al. 2012, A&A, 542, A29

Götberg, Y., de Mink, S. E., & Groh, J. H. 2017, A&A, 608, A11

Graur, O., Bianco, F. B., Modjaz, M., et al. 2017, ApJ, 837, 121

Groh, J. H., Meynet, G., & Ekström, S. 2013a, A&A, 550, L7

Groh, J. H., Meynet, G., Georgy, C., & Ekström, S. 2013b, A&A, 558, A131

Houck, J. C., & Fransson, C. 1996, ApJ, 456, 811

Iglesias, C. A., & Rogers, F. J. 1996, ApJ, 464, 943

Ivezic, Z., Tyson, J. A., Abel, B., et al. 2008, ArXiv e-prints, arXiv:0805.2366

Kamble, A., Margutti, R., Soderberg, A. M., et al. 2016, ApJ, 818, 111

Kilpatrick, C. D., Foley, R. J., Abramson, L. E., et al. 2017, MNRAS, 465, 4650

Kippenhahn, R., Ruschenplatt, G., & Thomas, H.-C. 1980, A&A, 91, 175

Kobulnicky, H. A., Kiminki, D. C., Lundquist, M. J., et al. 2014, ApJS, 213, 34

Kochanek, C. S. 2018, MNRAS, 473, 1633

Kochanek, C. S., Shappee, B. J., Stanek, K. Z., et al. 2017, PASP, 129, 104502

Köhler, K., Langer, N., de Koter, A., et al. 2015, A&A, 573, A71

Kolb, U., & Ritter, H. 1990, A&A, 236, 385

Krause, O., Birkmann, S. M., Usuda, T., et al. 2008, Science, 320, 1195

Krauss, M. I., Soderberg, A. M., Chomiuk, L., et al. 2012, ApJ, 750, L40

Kroupa, P. 2001, MNRAS, 322, 231

Langer, N. 1991, A&A, 252, 669

Langer, N., Fricke, K. J., & Sugimoto, D. 1983, A&A, 126, 207

Li, W., Chornock, R., Leaman, J., et al. 2011, MNRAS, 412, 1473

Liu, Y.-Q., Modjaz, M., Bianco, F. B., & Graur, O. 2016, ApJ, 827, 90

Lyman, J. D., Bersier, D., James, P. A., et al. 2016, MNRAS, 457, 328

Maeda, K., Hattori, T., Milisavljevic, D., et al. 2015, ApJ, 807, 35

Margutti, R., Chornock, R., Metzger, B. D., et al. 2017, ArXiv e-prints, arXiv:1704.05865

Maund, J. R., Smartt, S. J., Kudritzki, R. P., Podsiadlowski, P., & Gilmore, G. F. 2004, *Nature*, 427, 129

Maund, J. R., Fraser, M., Ergon, M., et al. 2011, ApJL, 739, L37

Moe, M., & Di Stefano, R. 2017, ApJS, 230, 15

Morales-Garoffolo, A., Elias-Rosa, N., Benetti, S., et al. 2014, MNRAS, 445, 1647

Moriya, T. J., Pruzhinskaya, M. V., Ergon, M., & Blinnikov, S. I. 2016, MNRAS, 455, 423

Nomoto, K., Suzuki, T., Shigeyama, T., et al. 1993, *Nature*, 364, 507

Nugis, T., & Lamers, H. J. G. L. M. 2000, A&A, 360, 227

Öpik, E. 1924, Publications of the Tartu Astrofizica Observatory, 25

Packet, W. 1981, A&A, 102, 17

Paxton, B., Bildsten, L., Dotter, A., et al. 2011, ApJS, 192, 3

Paxton, B., Cantiello, M., Arras, P., et al. 2013, ApJS, 208, 4

Paxton, B., Marchant, P., Schwab, J., et al. 2015, ApJS, 220, 15

Paxton, B., Schwab, J., Bauer, E. B., et al. 2018, ApJS, 234, 34

Peimbert, M., Luridiana, V., & Peimbert, A. 2007, ApJ, 666, 636

Petrovic, J., Langer, N., & van der Hucht, K. A. 2005, A&A, 435, 1013

Podsiadlowski, P., Hsu, J. J. L., Joss, P. C., & Ross, R. R. 1993, *Nature*, 364, 509

Podsiadlowski, P., Joss, P. C., & Hsu, J. J. L. 1992, ApJ, 391, 246

Popham, R., & Narayan, R. 1991, ApJ, 370, 604

Quataert, E., & Shiode, J. 2012, MNRAS, 423, L92

Rest, A., Foley, R. J., Sinnott, B., et al. 2011, ApJ, 732, doi:10.1088/0004-637X/732/1/3

Ritchie, B. W., Stroud, V. E., Evans, C. J., et al. 2012, A&A, 537, doi:10.1051/0004-6361/201117716

Ryder, S. D., Van Dyk, S. D., Fox, O. D., et al. 2018a, ArXiv e-prints, arXiv:1801.05125

—. 2018b, ApJ, 856, 83

Salpeter, E. E. 1955, ApJ, 121, 161

Sana, H., de Mink, S. E., de Koter, A., et al. 2012, Science, 337, 444

Schneider, F. R. N., Sana, H., Evans, C. J., et al. 2018, Science, 359, 69

Shiode, J. H., & Quataert, E. 2014, ApJ, 780, 96

Shivvers, I., Modjaz, M., Zheng, W., et al. 2017, PASP, 129, 054201

Smartt, S. J. 2009, ARA&A, 47, 63

Smith, N. 2014, ARA&A, 52, 487

Smith, N., Li, W., Filippenko, A. V., & Chornock, R. 2011, MNRAS, 412, 1522

Soderberg, A. M., Margutti, R., Zauderer, B. A., et al. 2012, ApJ, 752, 78

Soker, N. 2017, MNRAS, 470, L102

Sravan, N., Marchant, P., Kalogera, V., & Margutti, R. 2018, ApJL, 852, L17

Stancliffe, R. J., & Eldridge, J. J. 2009, MNRAS, 396, 1699

Stancliffe, R. J., Glebbeek, E., Izzard, R. G., & Pols, O. R. 2007, A&A, 464, L57

Strotjohann, N. L., Ofek, E. O., Gal-Yam, A., et al. 2015, ApJ, 811, 117

Tartaglia, L., Fraser, M., Sand, D. J., et al. 2017, ApJL, 836, L12

Tyson, J. A. 2002, in Proc. SPIE, Vol. 4836, Survey and Other Telescope Technologies and Discoveries, ed. J. A. Tyson & S. Wolff, 10–20

Vagnozzi, S., Freese, K., & Zurbuchen, T. H. 2017, ApJ, 839, 55

Valenti, S., David, Sand, J., et al. 2017, ApJL, 848, L24

Van Dyk, S. D., Li, W., Cenko, S. B., et al. 2011, ApJL, 741, L28

Van Dyk, S. D., Zheng, W., Fox, O. D., et al. 2014, AJ, 147, 37

Van Dyk, S. D., Zheng, W., Brink, T. G., et al. 2018, ArXiv e-prints, arXiv:1803.01050

Vink, J. S., de Koter, A., & Lamers, H. J. G. L. M. 2001, A&A, 369, 574

Vink, J. S., & Gräfener, G. 2012, ApJL, 751, L34

Wellons, S., Soderberg, A. M., & Chevalier, R. A. 2012, ApJ, 752, 17

Wellstein, S., Langer, N., & Braun, H. 2001, A&A, 369, 939

Woosley, S. E., Eastman, R. G., Weaver, T. A., & Pinto, P. A. 1994, ApJ, 429, 300

Woosley, S. E., Heger, A., & Weaver, T. A. 2002, Reviews of Modern Physics, 74, 1015

Woosley, S. E., Langer, N., & Weaver, T. A. 1993, ApJ, 411, 823

Yoon, S.-C., Dessart, L., & Clocchiatti, A. 2017, ApJ, 840, 10

Yoon, S.-C., Langer, N., & Norman, C. 2006, A&A, 460, 199

Yoon, S.-C., Woosley, S. E., & Langer, N. 2010, ApJ, 725, 940

APPENDIX A

Appendix

A.1. Numerical Tests

We stop the evolution of our single- and binary-star models close to core carbon depletion (according to the definitions in Section 2) and assume that their global characteristics of interest when investigating SN IIb progenitors are roughly the same until CC. To confirm that this is indeed the case, we run representative binary-star models at solar (case B mass transfer type) and low (also investigated in Section 4.2 and Figures 4.5 and 4.6) metallicity until central silicon mass fraction drops below 10^{-6} (at which point the models are a few hours from CC) and check whether the primary hydrogen envelope and helium core mass and H-R locations of both components differ significantly at this later evolutionary stage.

Figure A.1 shows the result of this test. We find that both models have converged by the fiducial evolutionary stopping criterion used in this work to that at the more advanced evolutionary stage for all properties relevant to our investigation.

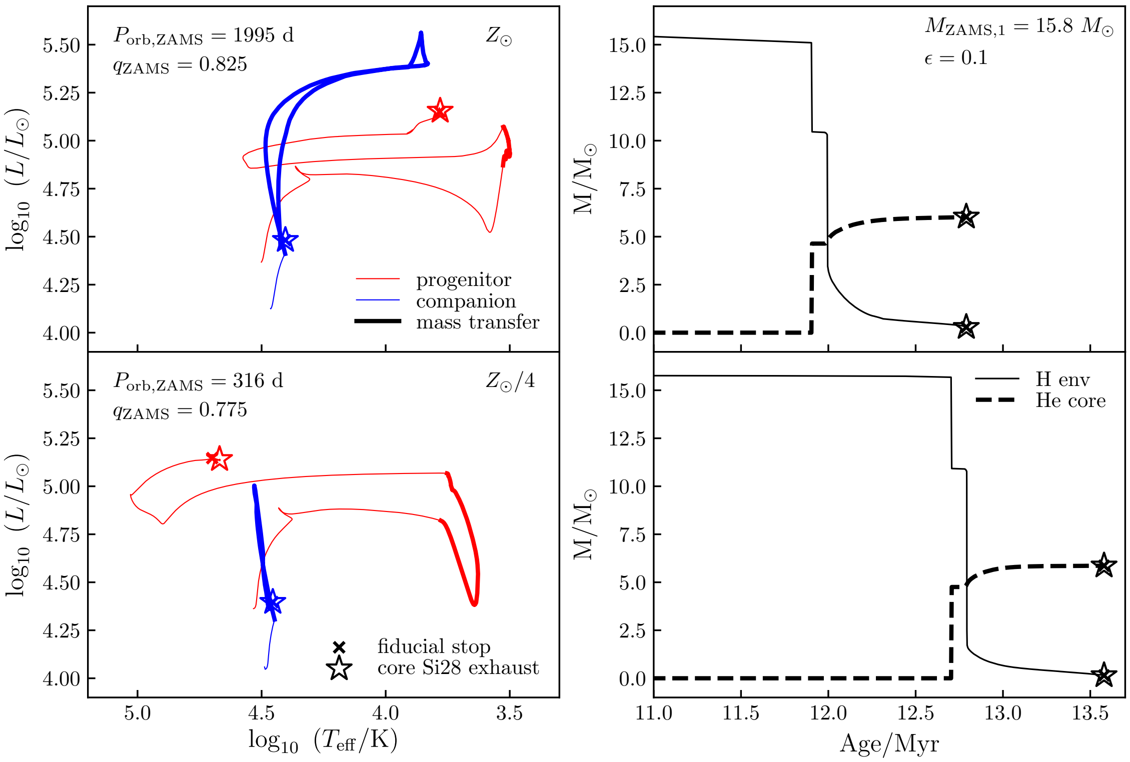

Figure A.1 *Left*: H-R diagrams showing evolution of representative solar- (top) and low- (bottom) metallicity binary-star models to core silicon exhaustion. Line colors and weights have the same meaning as in Figure 4.3. *Right*: Evolution of primary hydrogen envelope (solid line) and helium core mass (dashed line) as a function of binary age for the corresponding models on the left. In all panels, crosses (stars) denote the point carbon (silicon) is exhausted in the core of the corresponding binary component. The properties of all models have converged to those very near CC by the fiducial evolutionary stopping criterion used in this work.

Table A.1. SN IIb rates at solar metallicity

				$M_{\mathrm{He\ core}} \geq 0M_{\odot}$						$2M_{\odot} \leq M_{\mathrm{He\ core}} \leq 6M_{\odot}$					
				$M_{\mathrm{H\ env}} \leq 1.0M_{\odot}$			$M_{\mathrm{H\ env}} \leq 0.5M_{\odot}$			$M_{\mathrm{H\ env}} \leq 1.0M_{\odot}$			$M_{\mathrm{H\ env}} \leq 0.5M_{\odot}$		
f_{bin}	α	β	γ	single	binary		single	binary		single	binary		single	binary	
					$\epsilon = 0.5$	$\epsilon = 0.1$		$\epsilon = 0.5$	$\epsilon = 0.1$		$\epsilon = 0.5$	$\epsilon = 0.1$		$\epsilon = 0.5$	$\epsilon = 0.1$
0.25	1.6	-1.0	0.0	2.84	0.14	0.21	1.92	0.11	0.16	0.00	0.12	0.17	0.00	0.08	0.13
			-0.22	2.84	0.12	0.18	1.92	0.09	0.14	0.00	0.10	0.14	0.00	0.07	0.11
		0.0	0.0	2.84	0.20	0.33	1.92	0.14	0.26	0.00	0.16	0.26	0.00	0.10	0.20
			-0.22	2.84	0.17	0.28	1.92	0.12	0.22	0.00	0.13	0.22	0.00	0.09	0.17
	2.3	-1.0	0.0	2.83	0.22	0.31	1.88	0.16	0.24	0.00	0.18	0.26	0.00	0.13	0.20
			-0.22	2.83	0.18	0.27	1.88	0.13	0.21	0.00	0.15	0.23	0.00	0.11	0.17
		0.0	0.0	2.83	0.29	0.49	1.88	0.20	0.38	0.00	0.24	0.41	0.00	0.16	0.31

Table A.1 (cont'd)

f_{bin}	α	β	γ	$M_{He\ core} \geq 0M_\odot$						$2M_\odot \leq M_{He\ core} \leq 6M_\odot$					
				$M_{H\ env} \leq 1.0M_\odot$			$M_{H\ env} \leq 0.5M_\odot$			$M_{H\ env} \leq 1.0M_\odot$			$M_{H\ env} \leq 0.5M_\odot$		
				single	binary		single	binary		single	binary		single	binary	
					$\epsilon = 0.5$	$\epsilon = 0.1$		$\epsilon = 0.5$	$\epsilon = 0.1$		$\epsilon = 0.5$	$\epsilon = 0.1$		$\epsilon = 0.5$	$\epsilon = 0.1$
			-0.22	2.83	0.25	0.42	1.88	0.17	0.32	0.00	0.20	0.35	0.00	0.13	0.27
	3.0	-1.0	0.0	2.04	0.23	0.34	1.33	0.17	0.26	0.00	0.21	0.30	0.00	0.14	0.22
			-0.22	2.04	0.20	0.29	1.33	0.14	0.22	0.00	0.17	0.26	0.00	0.12	0.19
		0.0	0.0	2.04	0.32	0.53	1.33	0.22	0.41	0.00	0.27	0.46	0.00	0.18	0.35
			-0.22	2.04	0.27	0.46	1.33	0.18	0.35	0.00	0.23	0.40	0.00	0.15	0.30
	1.6	-1.0	0.0	1.58	0.24	0.35	1.07	0.18	0.27	0.00	0.20	0.28	0.00	0.14	0.21
			-0.22	1.58	0.20	0.30	1.07	0.15	0.23	0.00	0.17	0.24	0.00	0.12	0.18

Table A.1 (cont'd)

f_{bin}	α	β	γ	$M_{\mathrm{He\ core}} \geq 0M_\odot$						$2M_\odot \leq M_{\mathrm{He\ core}} \leq 6M_\odot$					
				$M_{\mathrm{H\ env}} \leq 1.0M_\odot$			$M_{\mathrm{H\ env}} \leq 0.5M_\odot$			$M_{\mathrm{H\ env}} \leq 1.0M_\odot$			$M_{\mathrm{H\ env}} \leq 0.5M_\odot$		
				single	binary		single	binary		single	binary		single	binary	
					$\epsilon = 0.5$	$\epsilon = 0.1$		$\epsilon = 0.5$	$\epsilon = 0.1$		$\epsilon = 0.5$	$\epsilon = 0.1$		$\epsilon = 0.5$	$\epsilon = 0.1$
0.50	2.3	0.0	0.0	1.58	0.33	0.55	1.07	0.24	0.43	0.00	0.26	0.44	0.00	0.17	0.33
			-0.22	1.58	0.28	0.47	1.07	0.20	0.37	0.00	0.22	0.37	0.00	0.15	0.29
		-1.0	0.0	1.57	0.36	0.52	1.04	0.26	0.40	0.00	0.30	0.44	0.00	0.21	0.33
			-0.22	**1.57**	**0.30**	**0.45**	1.04	0.22	0.34	0.00	0.26	0.38	0.00	0.18	0.28
		0.0	0.0	1.57	0.49	0.81	1.04	0.34	0.63	0.00	0.40	0.68	0.00	0.26	0.51
			-0.22	1.57	0.41	0.70	1.04	0.29	0.54	0.00	0.34	0.59	0.00	0.22	0.44
		-1.0	0.0	1.13	0.39	0.57	0.74	0.28	0.43	0.00	0.34	0.50	0.00	0.24	0.37

Table A.1 (cont'd)

f_{bin}	α	β	γ	$M_{\mathrm{He\ core}} \geq 0M_{\odot}$, $M_{\mathrm{H\ env}} \leq 1.0M_{\odot}$, single	binary $\epsilon = 0.5$	binary $\epsilon = 0.1$	$M_{\mathrm{H\ env}} \leq 0.5M_{\odot}$, single	binary $\epsilon = 0.5$	binary $\epsilon = 0.1$	$2M_{\odot} \leq M_{\mathrm{He\ core}} \leq 6M_{\odot}$, $M_{\mathrm{H\ env}} \leq 1.0M_{\odot}$, single	binary $\epsilon = 0.5$	binary $\epsilon = 0.1$	$M_{\mathrm{H\ env}} \leq 0.5M_{\odot}$, single	binary $\epsilon = 0.5$	binary $\epsilon = 0.1$
	3.0		-0.22	1.13	0.33	0.49	0.74	0.24	0.37	0.00	0.29	0.43	0.00	0.20	0.32
		0.0	0.0	1.13	0.53	0.89	0.74	0.36	0.68	0.00	0.45	0.77	0.00	0.29	0.58
			-0.22	1.13	0.45	0.76	0.74	0.31	0.59	0.00	0.38	0.67	0.00	0.25	0.50
	1.6	-1.0	0.0	1.00	0.29	0.41	0.68	0.21	0.32	0.00	0.23	0.33	0.00	0.16	0.25
			-0.22	1.00	0.24	0.35	0.68	0.18	0.28	0.00	0.20	0.28	0.00	0.14	0.21
		0.0	0.0	1.00	0.39	0.64	0.68	0.28	0.50	0.00	0.31	0.51	0.00	0.20	0.39
			-0.22	1.00	0.33	0.55	0.68	0.24	0.43	0.00	0.26	0.44	0.00	0.17	0.34

Table A.1 (cont'd)

				$M_{\mathrm{He\ core}} \geq 0M_\odot$						$2M_\odot \leq M_{\mathrm{He\ core}} \leq 6M_\odot$					
				$M_{\mathrm{H\ env}} \leq 1.0M_\odot$			$M_{\mathrm{H\ env}} \leq 0.5M_\odot$			$M_{\mathrm{H\ env}} \leq 1.0M_\odot$			$M_{\mathrm{H\ env}} \leq 0.5M_\odot$		
f_{bin}	α	β	γ	single	binary		single	binary		single	binary		single	binary	
					$\epsilon = 0.5$	$\epsilon = 0.1$		$\epsilon = 0.5$	$\epsilon = 0.1$		$\epsilon = 0.5$	$\epsilon = 0.1$		$\epsilon = 0.5$	$\epsilon = 0.1$
0.65	2.3	-1.0	0.0	1.00	0.42	0.62	0.66	0.31	0.47	0.00	0.36	0.52	0.00	0.25	0.39
			-0.22	1.00	0.36	0.53	0.66	0.26	0.41	0.00	0.30	0.44	0.00	0.22	0.33
		0.0	0.0	1.00	0.58	0.96	0.66	0.40	0.74	0.00	0.47	0.81	0.00	0.31	0.61
			-0.22	1.00	0.49	0.83	0.66	0.34	0.64	0.00	0.40	0.69	0.00	0.27	0.52
	3.0	-1.0	0.0	0.72	0.46	0.67	0.47	0.33	0.51	0.00	0.40	0.59	0.00	0.28	0.43
			-0.22	0.72	0.39	0.58	0.47	0.28	0.44	0.00	0.34	0.50	0.00	0.24	0.38
		0.0	0.0	0.72	0.62	1.05	0.47	0.43	0.80	0.00	0.53	0.91	0.00	0.35	0.69

Table A.1 (cont'd)

f_{bin}	α	β	γ	$M_{He\ core} \geq 0M_\odot$						$2M_\odot \leq M_{He\ core} \leq 6M_\odot$					
				$M_{H\ env} \leq 1.0M_\odot$			$M_{H\ env} \leq 0.5M_\odot$			$M_{H\ env} \leq 1.0M_\odot$			$M_{H\ env} \leq 0.5M_\odot$		
				single	binary		single	binary		single	binary		single	binary	
					$\epsilon = 0.5$	$\epsilon = 0.1$		$\epsilon = 0.5$	$\epsilon = 0.1$		$\epsilon = 0.5$	$\epsilon = 0.1$		$\epsilon = 0.5$	$\epsilon = 0.1$
			-0.22	0.72	0.53	0.90	0.47	0.36	0.69	0.00	0.45	0.79	0.00	0.29	0.59
	1.6	-1.0	0.0	0.53	0.32	0.47	0.36	0.24	0.36	0.00	0.26	0.37	0.00	0.19	0.28
			-0.22	0.53	0.27	0.40	0.36	0.20	0.31	0.00	0.22	0.32	0.00	0.16	0.24
		0.0	0.0	0.53	0.44	0.73	0.36	0.31	0.57	0.00	0.34	0.58	0.00	0.23	0.44
			-0.22	0.53	0.37	0.62	0.36	0.27	0.49	0.00	0.29	0.50	0.00	0.20	0.38
0.80	2.3	-1.0	0.0	0.52	0.48	0.69	0.35	0.35	0.53	0.00	0.41	0.58	0.00	0.29	0.44
			-0.22	0.52	0.41	0.59	0.35	0.30	0.46	0.00	0.34	0.50	0.00	0.24	0.38

Table A.1 (cont'd)

f_{bin}	α	β	γ	$M_{He\ core} \geq 0M_\odot$						$2M_\odot \leq M_{He\ core} \leq 6M_\odot$					
				$M_{H\ env} \leq 1.0M_\odot$			$M_{H\ env} \leq 0.5M_\odot$			$M_{H\ env} \leq 1.0M_\odot$			$M_{H\ env} \leq 0.5M_\odot$		
				single	binary		single	binary		single	binary		single	binary	
					$\epsilon = 0.5$	$\epsilon = 0.1$		$\epsilon = 0.5$	$\epsilon = 0.1$		$\epsilon = 0.5$	$\epsilon = 0.1$		$\epsilon = 0.5$	$\epsilon = 0.1$
		0.0	0.0	0.52	0.65	1.08	0.35	0.45	0.84	0.00	0.53	0.91	0.00	0.35	0.69
			-0.22	0.52	0.55	0.93	0.35	0.39	0.72	0.00	0.45	0.78	0.00	0.30	0.59
	3.0	-1.0	0.0	0.38	0.52	0.76	0.25	0.38	0.58	0.00	0.46	0.66	0.00	0.32	0.49
			-0.22	0.38	0.44	0.65	0.25	0.32	0.50	0.00	0.39	0.57	0.00	0.27	0.42
		0.0	0.0	0.38	0.70	1.18	0.25	0.48	0.91	0.00	0.60	1.03	0.00	0.39	0.77
			-0.22	0.38	0.59	1.02	0.25	0.41	0.78	0.00	0.51	0.89	0.00	0.33	0.67

[1] $M_{He\ core} \equiv M_{He\ core,preSN(,1)}$: Residual hydrogen envelope mass in the progenitor at CC

[2] $M_{H\ env} \equiv M_{H\ env,preSN(,1)}$: Helium core mass of the progenitor at CC

Note. — f_{bin} is fraction of binary systems and α, β, and γ are parameters for the priors on the initial mass, $\log_{10} M_{ZAMS}$, initial mass ratio, q_{ZAMS}, and initial orbital period, P_{orb}, respectively (see Eqs. 3.1, 3.2, and 3.3). SN IIb rate is defined as fraction of SNe IIb vs all CC SNe percent. Values in boldface are for our fiducial values of f_{bin}, α, β, and γ and fiducial definition of SN IIb progenitors (see Section 3).

Table A.2. SN IIb rates at low metallicity

				$M_{\mathrm{He\ core}} \geq 0M_\odot$						$2M_\odot \leq M_{\mathrm{He\ core}} \leq 6M_\odot$					
				$M_{\mathrm{H\ env}} \leq 1.0M_\odot$			$M_{\mathrm{H\ env}} \leq 0.5M_\odot$			$M_{\mathrm{H\ env}} \leq 1.0M_\odot$			$M_{\mathrm{H\ env}} \leq 0.5M_\odot$		
f_{bin}	α	β	γ	single	binary		single	binary		single	binary		single	binary	
					$\epsilon = 0.5$	$\epsilon = 0.1$		$\epsilon = 0.5$	$\epsilon = 0.1$		$\epsilon = 0.5$	$\epsilon = 0.1$		$\epsilon = 0.5$	$\epsilon = 0.1$
0.25	1.6	-1.0	0.0	2.19	0.41	1.67	–	0.34	1.55	0.00	0.32	1.34	0.00	0.29	1.28
			-0.22	2.19	0.40	1.60	–	0.34	1.51	0.00	0.32	1.30	0.00	0.30	1.25
		0.0	0.0	2.19	0.65	2.16	–	0.56	1.98	0.00	0.52	1.71	0.00	0.48	1.61
			-0.22	2.19	0.64	2.07	–	0.57	1.92	0.00	0.52	1.66	0.00	0.49	1.57
	2.3	-1.0	0.0	1.25	0.62	2.52	–	0.53	2.36	0.00	0.52	2.12	0.00	0.47	2.02
			-0.22	1.25	0.62	2.43	–	0.54	2.29	0.00	0.52	2.06	0.00	0.48	1.97
		0.0	0.0	1.25	0.99	3.25	–	0.88	3.00	0.00	0.84	2.70	0.00	0.79	2.54

Table A.2 (cont'd)

$f_{\rm bin}$	α	β	γ	$M_{\rm He\ core} \geq 0M_{\odot}$						$2M_{\odot} \leq M_{\rm He\ core} \leq 6M_{\odot}$					
				$M_{\rm H\ env} \leq 1.0M_{\odot}$			$M_{\rm H\ env} \leq 0.5M_{\odot}$			$M_{\rm H\ env} \leq 1.0M_{\odot}$			$M_{\rm H\ env} \leq 0.5M_{\odot}$		
				single	binary		single	binary		single	binary		single	binary	
					$\epsilon = 0.5$	$\epsilon = 0.1$		$\epsilon = 0.5$	$\epsilon = 0.1$		$\epsilon = 0.5$	$\epsilon = 0.1$		$\epsilon = 0.5$	$\epsilon = 0.1$
			-0.22	1.25	0.99	3.13	–	0.89	2.91	0.00	0.85	2.62	0.00	0.80	2.48
	3.0	-1.0	0.0	0.51	0.70	2.79	–	0.61	2.62	0.00	0.61	2.43	0.00	0.56	2.32
			-0.22	0.51	0.70	2.69	–	0.62	2.55	0.00	0.61	2.37	0.00	0.57	2.27
		0.0	0.0	0.51	1.12	3.59	–	1.01	3.32	0.00	0.99	3.10	0.00	0.93	2.91
			-0.22	0.51	1.12	3.45	–	1.03	3.22	0.00	1.00	3.01	0.00	0.95	2.84
	1.6	-1.0	0.0	1.46	0.68	2.78	–	0.57	2.59	0.00	0.53	2.23	0.00	0.49	2.13
			-0.22	1.46	0.67	2.67	–	0.57	2.51	0.00	0.54	2.17	0.00	0.50	2.08

Table A.2 (cont'd)

$f_{\rm bin}$	α	β	γ	$M_{\rm He\ core} \geq 0M_\odot$						$2M_\odot \leq M_{\rm He\ core} \leq 6M_\odot$					
				$M_{\rm H\ env} \leq 1.0M_\odot$			$M_{\rm H\ env} \leq 0.5M_\odot$			$M_{\rm H\ env} \leq 1.0M_\odot$			$M_{\rm H\ env} \leq 0.5M_\odot$		
				single	binary		single	binary		single	binary		single	binary	
					$\epsilon = 0.5$	$\epsilon = 0.1$		$\epsilon = 0.5$	$\epsilon = 0.1$		$\epsilon = 0.5$	$\epsilon = 0.1$		$\epsilon = 0.5$	$\epsilon = 0.1$
0.50	2.3	0.0	0.0	1.46	1.08	3.61	–	0.93	3.30	0.00	0.86	2.85	0.00	0.81	2.68
			-0.22	1.46	1.07	3.46	–	0.95	3.20	0.00	0.87	2.76	0.00	0.82	2.62
		-1.0	0.0	0.83	1.04	4.20	–	0.89	3.93	0.00	0.86	3.53	0.00	0.79	3.36
			-0.22	**0.83**	**1.03**	**4.05**	–	0.90	3.82	0.00	0.87	3.43	0.00	0.81	3.29
		0.0	0.0	0.83	1.66	5.42	–	1.46	5.00	0.00	1.39	4.50	0.00	1.31	4.23
			-0.22	0.83	1.65	5.21	–	1.49	4.84	0.00	1.41	4.36	0.00	1.34	4.13
		-1.0	0.0	0.34	1.17	4.64	–	1.02	4.37	0.00	1.02	4.06	0.00	0.94	3.86

Table A.2 (cont'd)

$f_{\rm bin}$	α	β	γ	$M_{\rm He\ core} \geq 0M_\odot$						$2M_\odot \leq M_{\rm He\ core} \leq 6M_\odot$					
				$M_{\rm H\ env} \leq 1.0M_\odot$			$M_{\rm H\ env} \leq 0.5M_\odot$			$M_{\rm H\ env} \leq 1.0M_\odot$			$M_{\rm H\ env} \leq 0.5M_\odot$		
				single	binary		single	binary		single	binary		single	binary	
					$\epsilon = 0.5$	$\epsilon = 0.1$		$\epsilon = 0.5$	$\epsilon = 0.1$		$\epsilon = 0.5$	$\epsilon = 0.1$		$\epsilon = 0.5$	$\epsilon = 0.1$
	3.0		-0.22	0.34	1.16	4.49	–	1.04	4.25	0.00	1.02	3.94	0.00	0.96	3.78
		0.0	0.0	0.34	1.87	5.98	–	1.68	5.53	0.00	1.64	5.17	0.00	1.55	4.86
			-0.22	0.34	1.87	5.76	–	1.71	5.37	0.00	1.66	5.01	0.00	1.58	4.74
	1.6	-1.0	0.0	1.02	0.81	3.28	–	0.67	3.06	0.00	0.63	2.64	0.00	0.57	2.52
			-0.22	1.02	0.79	3.16	–	0.68	2.97	0.00	0.63	2.56	0.00	0.59	2.46
		0.0	0.0	1.02	1.28	4.26	–	1.10	3.90	0.00	1.02	3.37	0.00	0.95	3.17
			-0.22	1.02	1.27	4.08	–	1.12	3.78	0.00	1.03	3.26	0.00	0.97	3.09

Table A.2 (cont'd)

$f_{\rm bin}$	α	β	γ	$M_{\rm He\ core} \geq 0M_\odot$						$2M_\odot \leq M_{\rm He\ core} \leq 6M_\odot$					
				$M_{\rm H\ env} \leq 1.0M_\odot$			$M_{\rm H\ env} \leq 0.5M_\odot$			$M_{\rm H\ env} \leq 1.0M_\odot$			$M_{\rm H\ env} \leq 0.5M_\odot$		
				single	binary		single	binary		single	binary		single	binary	
					$\epsilon = 0.5$	$\epsilon = 0.1$		$\epsilon = 0.5$	$\epsilon = 0.1$		$\epsilon = 0.5$	$\epsilon = 0.1$		$\epsilon = 0.5$	$\epsilon = 0.1$
0.65	2.3	-1.0	0.0	0.58	1.23	4.96	–	1.05	4.65	0.00	1.02	4.17	0.00	0.93	3.98
			-0.22	0.58	1.22	4.78	–	1.07	4.51	0.00	1.03	4.05	0.00	0.95	3.89
		0.0	0.0	0.58	1.96	6.41	–	1.73	5.90	0.00	1.65	5.32	0.00	1.55	5.00
			-0.22	0.58	1.95	6.16	–	1.76	5.72	0.00	1.67	5.16	0.00	1.58	4.88
	3.0	-1.0	0.0	0.24	1.38	5.49	–	1.21	5.16	0.00	1.20	4.79	0.00	1.11	4.57
			-0.22	0.24	1.37	5.31	–	1.23	5.02	0.00	1.21	4.66	0.00	1.13	4.46
		0.0	0.0	0.24	2.21	7.07	–	1.99	6.54	0.00	1.94	6.11	0.00	1.83	5.74

Table A.2 (cont'd)

f_{bin}	α	β	γ	$M_{He\ core} \geq 0M_{\odot}$						$2M_{\odot} \leq M_{He\ core} \leq 6M_{\odot}$					
				$M_{H\ env} \leq 1.0M_{\odot}$			$M_{H\ env} \leq 0.5M_{\odot}$			$M_{H\ env} \leq 1.0M_{\odot}$			$M_{H\ env} \leq 0.5M_{\odot}$		
				single	binary		single	binary		single	binary		single	binary	
					$\epsilon = 0.5$	$\epsilon = 0.1$		$\epsilon = 0.5$	$\epsilon = 0.1$		$\epsilon = 0.5$	$\epsilon = 0.1$		$\epsilon = 0.5$	$\epsilon = 0.1$
			-0.22	0.24	2.21	6.80	–	2.02	6.35	0.00	1.96	5.92	0.00	1.87	5.60
	1.6	-1.0	0.0	0.58	0.91	3.70	–	0.76	3.45	0.00	0.71	2.98	0.00	0.65	2.84
			-0.22	0.58	0.90	3.57	–	0.77	3.35	0.00	0.71	2.89	0.00	0.66	2.77
		0.0	0.0	0.58	1.44	4.81	–	1.24	4.40	0.00	1.15	3.80	0.00	1.07	3.58
			-0.22	0.58	1.43	4.61	–	1.26	4.26	0.00	1.16	3.68	0.00	1.10	3.49
0.80	2.3	-1.0	0.0	0.33	1.39	5.59	–	1.19	5.24	0.00	1.15	4.71	0.00	1.05	4.49
			-0.22	0.33	1.37	5.40	–	1.20	5.09	0.00	1.16	4.57	0.00	1.08	4.38

Table A.2 (cont'd)

f_{bin}	α	β	γ	$M_{He\ core} \geq 0M_\odot$						$2M_\odot \leq M_{He\ core} \leq 6M_\odot$					
				$M_{H\ env} \leq 1.0M_\odot$			$M_{H\ env} \leq 0.5M_\odot$			$M_{H\ env} \leq 1.0M_\odot$			$M_{H\ env} \leq 0.5M_\odot$		
				single	binary		single	binary		single	binary		single	binary	
					$\epsilon = 0.5$	$\epsilon = 0.1$		$\epsilon = 0.5$	$\epsilon = 0.1$		$\epsilon = 0.5$	$\epsilon = 0.1$		$\epsilon = 0.5$	$\epsilon = 0.1$
		0.0	0.0	0.33	2.21	7.23	–	1.95	6.66	0.00	1.86	6.01	0.00	1.75	5.64
			-0.22	0.33	2.20	6.95	–	1.98	6.46	0.00	1.88	5.82	0.00	1.78	5.50
	3.0	-1.0	0.0	0.14	1.56	6.19	–	1.36	5.82	0.00	1.35	5.41	0.00	1.25	5.15
			-0.22	0.14	1.55	5.99	–	1.38	5.67	0.00	1.36	5.26	0.00	1.27	5.04
		0.0	0.0	0.14	2.49	7.97	–	2.24	7.38	0.00	2.19	6.90	0.00	2.06	6.47
			-0.22	0.14	2.49	7.68	–	2.28	7.16	0.00	2.21	6.68	0.00	2.11	6.31

Note. — Table notes and notation same as in Table A.1.

Table A.3. SN IIb rates at solar and low metallicities from distributions of Moe & Di Stefano (2017)

		$M_{\mathrm{He\ core}} \geq 0M_{\odot}$						$2M_{\odot} \leq M_{\mathrm{He\ core}} \leq 6M_{\odot}$					
		$M_{\mathrm{H\ env}} \leq 1.0M_{\odot}$			$M_{\mathrm{H\ env}} \leq 0.5M_{\odot}$			$M_{\mathrm{H\ env}} \leq 1.0M_{\odot}$			$M_{\mathrm{H\ env}} \leq 0.5M_{\odot}$		
Z	α	single	binary		single	binary		single	binary		single	binary	
			$\epsilon = 0.5$	$\epsilon = 0.1$		$\epsilon = 0.5$	$\epsilon = 0.1$		$\epsilon = 0.5$	$\epsilon = 0.1$		$\epsilon = 0.5$	$\epsilon = 0.1$
	1.6	0.21 − 0.40	0.12 − 0.22	0.15 − 0.29	0.14 − 0.26	0.09 − 0.17	0.12 − 0.22	0.00	0.10 − 0.19	0.12 − 0.24	0.00	0.07 − 0.14	0.09 − 0.17
$Z_{\odot}$	2.3	0.18 − 0.33	0.15 − 0.28	0.20 − 0.37	0.11 − 0.22	0.11 − 0.21	0.15 − 0.28	0.00	0.13 − 0.25	0.17 − 0.32	0.00	0.10 − 0.18	0.13 − 0.24
	3.0	0.13 − 0.24	0.16 − 0.30	0.22 − 0.41	0.08 − 0.15	0.12 − 0.23	0.17 − 0.31	0.00	0.14 − 0.27	0.19 − 0.36	0.00	0.11 − 0.20	0.14 − 0.26
	1.6	0.01 − 0.02	0.51 − 0.98	1.73 − 3.32	–	0.46 − 0.88	1.66 − 3.18	0.00	0.42 − 0.80	1.41 − 2.70	0.00	0.40 − 0.76	1.37 − 2.63
$\frac{Z_{\odot}}{4}$	2.3	0.00 − 0.01	0.70 − 1.31	2.32 − 4.38	–	0.63 − 1.20	2.23 − 4.20	0.00	0.59 − 1.12	1.97 − 3.70	0.00	0.56 − 1.06	1.90 − 3.59
	3.0	0.00	0.80 − 1.49	2.56 − 4.77	–	0.74 − 1.38	2.46 − 4.58	0.00	0.71 − 1.32	2.24 − 4.18	0.00	0.68 − 1.26	2.17 − 4.05

Note. — Table notes and notation same as in Table A.1. The lower (upper) limit on rates is from assuming that all (none) of the secondaries explode as SNe.

SN IIb rates at solar and low metallicities using 10^6 single and binary stars generated from distributions of Moe & Di Stefano (2017)